

Recent Hadley Circulation Strengthening: A Trend or Multidecadal Variability?

ŽIGA ZAPLOTNIK,^a MATIC PIKOVNIK,^a AND LINA BOLJKA^b

^a Faculty of Mathematics and Physics, University of Ljubljana, Ljubljana, Slovenia

^b Geophysical Institute, University of Bergen and Bjerknes Centre for Climate Research, Bergen, Norway

(Manuscript received 13 March 2021, in final form 24 December 2021)

ABSTRACT: This study explores the possible drivers of the recent Hadley circulation strengthening in the modern reanalyses. Predominantly, two recent generations of reanalyses provided by the European Centre for Medium-Range Weather Forecasts are used: the fifth-generation atmospheric reanalysis (ERA5) and the interim reanalysis (ERA-Interim). Some results are also evaluated against other long-term reanalyses. To assess the origins of the Hadley cell (HC) strength variability, we employ the Kuo–Eliassen (KE) equation. ERA5 shows that both HCs were strengthening prior to the 2000s, but they have been weakening or remained steady afterward. Most of the long-term variability in the strength of the HCs is explained by the meridional gradient of diabatic (latent) heating, which is related to precipitation gradients. However, the strengthening of both HCs in ERA5 is larger than the strengthening expected from the observed zonal-mean precipitation gradient [estimated from the Global Precipitation Climatology Project (GPCP)]. This suggests that the HC strength trends in the recent decades in ERA5 can be explained partly as an artifact of the misrepresentation of latent heating and partly through (physical) long-term variability. To show that the latter is true, we analyze ERA5 preliminary data for the 1950–78 period, other long-term (e.g., twentieth century) reanalyses, and sea surface temperature observational data. This reveals that the changes in the HC strength can be a consequence of the Atlantic multidecadal oscillation (AMO) and related diabatic and frictional processes, which in turn drive the global HC variability. This work has implications for further understanding of the long-term variability of the Hadley circulation.


KEYWORDS: Tropics; Atmospheric circulation; Hadley circulation; Streamfunction; North Atlantic Oscillation; Pacific decadal oscillation; Sea surface temperature; Reanalysis data; Decadal variability; Multidecadal variability; Trends


1. Introduction

The thermodynamic effects of the increasing atmospheric greenhouse gas concentrations on the global-mean surface temperature have been accurately predicted by climate models, as shown by comparisons of past model projections and observations (Hausfather et al. 2020). However, the future projections of the atmospheric circulation changes remain less clear (Shepherd 2014). For example, studies have shown opposing Hadley circulation trends in the climate models and the reanalyses (e.g., Chemke and Polvani 2019). On the one hand, climate model projections show robust weakening of the northern Hadley cell (NHC) (e.g., Vallis et al. 2015; Hu et al. 2018; Xia et al. 2020) and minor strengthening of the southern Hadley cell (SHC) by the end of the twenty-first century (Ma and Xie 2013; Xia et al. 2020). On the other hand, both observations and global atmospheric reanalyses mostly show intensification of the Hadley cells (HCs) in the recent decades (Tanaka et al. 2004; Mitas and Clement 2005; Sohn and Park 2010; Stachnik and Schumacher 2011; Nguyen

et al. 2013; Chemke and Polvani 2019; Pikovnik et al. 2021). Nevertheless, the consensus on the projected future long-term weakening of the NHC has been unequivocal to date, supported by simulations from phases 5 and 6 of the Coupled Model Intercomparison Project (CMIP5 and CMIP6; Xia et al. 2020).

The drivers of the recent and future changes in the HC strength are yet to be fully explained. Many potential mechanisms have been suggested as explanations for the weakening of the circulation, such as the reduced differential diabatic heating between the ascending and descending branches of the HC due to a direct impact of spatially inhomogeneous changes of CO₂-induced radiative forcing (Merlis 2015; Xia and Huang 2017; Stuecker et al. 2020). Other modeling results suggest that the primary factors governing the weakening of the NHC are weaker zonal-mean meridional temperature gradients in the atmosphere and ocean; that is, the northern subtropical oceans warm more than the equatorial oceans (Seo et al. 2014; Gastineau et al. 2009; Burls and Fedorov 2017). On the other hand, reduced warming in the southern subtropical oceans relative to the tropical oceans would strengthen the SHC. Projected sea surface temperature (SST) changes are thus considered to be one of the largest sources of uncertainty in the future changes of the HC strength (Gastineau et al. 2009; Kang et al. 2013; Ma and Xie 2013). This is expected since the SSTs adjust to the dominant ocean heat transport in the low latitudes. Recently, it has also been shown that the ocean heat transport reduces the weakening of the circulation by 60% (Chemke 2021), a finding similar to the results of Levine and Schneider (2011). Nevertheless,

 Denotes content that is immediately available upon publication as open access.

 Supplemental information related to this paper is available at the Journals Online website: <https://doi.org/10.1175/JCLI-D-21-0204.s1>.

Corresponding author: Žiga Zaplotnik, ziga.zaplotnik@mf.uni-lj.si

DOI: 10.1175/JCLI-D-21-0204.1

© 2022 American Meteorological Society. For information regarding reuse of this content and general copyright information, consult the [AMS Copyright Policy \(www.ametsoc.org/PUBSReuseLicenses\)](#).

there is a growing consensus that the main driver of the NHC weakening is the increase in the static stability (Knutson and Manabe 1995; Lu et al. 2008; Bony et al. 2013; Chou et al. 2013; Vallis et al. 2015; Chemke and Polvani 2019, 2020). However, none of the aforementioned mechanisms alone can fully explain the changes in the HC strength as all these processes are strongly coupled within the climate system (Chemke and Polvani 2020).

The discrepancy in the HC strength between climate models and reanalyses has been often attributed to artifacts in the representation of latent heating in the reanalyses (Held and Soden 2006; Chemke and Polvani 2019) rather than to long-term variability. However, it has been suggested recently that the ensemble means of the fully coupled climate models do not reproduce some observed features of the tropical circulation (while some members of the large ensemble do), suggesting a possible major role of internal variability or significant model biases. Such examples include 1) the strengthening of the equatorial Pacific zonal SST gradient in the past decades, which affects the Pacific Walker circulation (Luo et al. 2018; Chung et al. 2019; Seager et al. 2019; Watanabe et al. 2020), and 2) the pronounced strengthening of the Pacific trade winds (related to the first point) and thus enhanced upwelling of the cold water in the eastern Pacific (La Niña-like conditions), which contributed to the so-called global warming hiatus in the 2000s (Trenberth and Fasullo 2013; England et al. 2014). Recent studies have also suggested that the observed widening of the Hadley circulation is an aggregate result of CO₂ forcing and long-term variability (Vaughn et al. 2018), such as the Pacific decadal oscillation (PDO; Allen and Kovilakam 2017; Grise et al. 2019). Moreover, the Atlantic multidecadal oscillation (AMO), defined by the SST variability in the North Atlantic (Kerr 2000; Enfield et al. 2001), modifies the Atlantic–Pacific interbasin pressure differences and drives the interbasin teleconnections, resulting in multiple changes in the tropical circulation. For example, McGregor et al. (2014) and Li et al. (2016) have demonstrated that the AMO-induced Atlantic SST anomalies affect the trade winds and the Walker circulation, while Levine et al. (2018) have confirmed the connection between the AMO and the long-term variability in the meridional shifts of the intertropical convergence zone (ITCZ).

Given the above examples from the recently published studies, we investigate here whether the recent (1979–2018) trends in the HC strength in reanalyses are an artifact or an observed part of the decadal–multidecadal climate variability. This 40-yr period is initially used as the satellite observations of the precipitation exist only for this period [e.g., the Global Precipitation Climatology Project (GPCP)]. We first analyze the changes in the strength of the NHC and SHC using the state-of-the-art fifth-generation atmospheric reanalysis (ERA5; Hersbach et al. 2020) provided by the European Centre for Medium-Range Weather Forecasts (ECMWF), and compare the results to the ECMWF's interim reanalysis (ERA-Interim; Dee et al. 2011) (section 3). We perform the analysis by solving the Kuo–Eliassen equation without quasigeostrophic assumptions, which allows us to attribute changes in the HC strength to different physical mechanisms

that affect the Hadley circulation. The changes in the HC strength and the main contributing mechanisms to these changes are then compared with the changes in precipitation (from reanalyses and other observational datasets) to assess if the HC trends are artifacts. Finally, the changes in the HC strength in ERA5, ERA-Interim, and four additional reanalyses (ERA-20C, CERA-20C, NOAA-20CRv3, and NCEP–NCAR) are compared with the indices of interannual–multidecadal variability over extended periods ranging from 1870 to the present as available (see section 4).

This study is organized as follows. Section 2 describes the data, methods, and theory. Sections 3 and 4 provide the analysis and the results (as mentioned above). Conclusions are given in section 5.

2. Data and methods

a. Data

1) REANALYSIS AND SST DATA

Reanalyses are retrospective analyses of the past global weather patterns using the latest forecasting models. They are produced by assimilating observed data in the dynamical forecasting model in successive time windows. Six modern reanalyses are used in this study: the ERA5 (Hersbach et al. 2020), ERA-Interim (Dee et al. 2011), ERA-20C (Poli et al. 2016), CERA-20C (Laloyaux et al. 2018), NOAA-20CRv3 (Slivinski et al. 2021), and NCEP–NCAR reanalyses (Kalnay et al. 1996). The drivers of the HC strength are examined in detail only for ERA5 and ERA-Interim, whereas the HC strength is computed and compared to decadal–multidecadal indices for all six reanalyses.

Compared to ERA-Interim, ERA5 has a higher model resolution (0.3° compared with 1° in ERA-Interim) and improvements in the dynamical core, model physics, and data assimilation procedures (Hersbach et al. 2020). Apart from the model improvements, ERA5 benefits also from 5 times more assimilated data. ERA5 incorporates the changes in the radiative forcing from CMIP5 [i.e., the evolution of greenhouse gases and aerosols (e.g., due to volcanic eruptions)] and includes state-of-the-art SST and sea ice concentration (SIC) data in order to capture the low-frequency variability of the climate system better. Altogether, these upgrades result in a better agreement with the observations of tropospheric temperature, wind, and humidity, as well as surface precipitation. For example, global-mean correlation with monthly mean GPCP data has increased from 67% for ERA-Interim to 77% for ERA5 (Hersbach et al. 2020). An important feature for the HC estimation is that ERA5 also significantly reduces surface meridional wind and horizontal wind divergence bias over the oceans (Rivas and Stoffelen 2019). Given these advantages of ERA5, we consider it as our main dataset in this study.

To examine the drivers of the HC strength, we analyze 40 years (1979–2018) of daily data at 0000 UTC. Temperature T , zonal wind u , meridional wind v , and pressure velocity ω (in units of Pa s⁻¹) are analyzed on standard 37 pressure levels on the latitude–longitude grid with 1° resolution for both

reanalyses. The budget terms (i.e., 100 and 1000; see below) are computed at the daily resolution, and ultimately seasonal and annual means are obtained for comparisons, as well as for visualization and smoothing purposes. ERA5 and ERA-Interim monthly precipitation data were obtained at 0.25° and 1° resolution, respectively.

For comparison with the decadal–multidecadal indices, we use preliminary extended ERA5 data (1950–78 in addition to 1979–2018) to capture the full cycles of various indices. Monthly mean meridional wind data are used to compute the streamfunction and to derive the HC strength. ERA-20C and CERA-20C data for the 1901–2010 period are analyzed at 1° spatial resolution and standard 37 pressure levels. NOAA-20CRv3 reanalysis data for the 1836–2015 period are also analyzed at 1° resolution and 28 pressure levels, whereas NCEP–NCAR reanalysis data are used at coarser 2.5° resolution and 17 pressure levels for the 1948–2018 period.

We also analyze the relationship between the Hadley cell strength and the SSTs. For this we use the HadISST dataset (Rayner et al. 2003) that was linearly detrended based on the period 1870–2018 for consistency with the interannual–multidecadal indices (see below).

2) PRECIPITATION MEASUREMENTS

Monthly mean precipitation estimates at 2.5° resolution were obtained from GPCP version 2.3 (Adler et al. 2018) for the same 1979–2018 period. The GPCP data combine satellite microwave and IR imagery and surface rain gauge data from Global Precipitation Climatology Centre (GPCC) (Schneider et al. 2017). Tropical Rainfall Measuring Mission (TRMM) data for the 1998–2018 period (Huffman et al. 2019) were obtained at 0.25° resolution (available only in the 50°S–50°N belt). TRMM combines radar measurements, microwave imagery, IR scanners, spectrometers, and lightning data.

Note that GPCP and TRMM datasets are not perfectly independent from reanalyses. The latter also use precipitation information by assimilating the same satellite products (from microwave imagery, radar reflectivity, etc.) as the precipitation datasets, although in a slightly different manner.

3) INDICES OF INTERANNUAL-TO-MULTIDECADAL VARIABILITY

The strength of the HC and some other related measures are compared with four SST-based indices of interannual-to-multidecadal variability: El Niño–Southern Oscillation (ENSO; e.g., Wang et al. 2017) in the Niño-3.4 region, the Pacific decadal oscillation (PDO; e.g., Newman et al. 2016), the interdecadal Pacific oscillation (IPO) computed via the tripole index (TPI) (e.g., Henley et al. 2015), and Atlantic multidecadal oscillation (AMO; e.g., Kerr 2000; Enfield et al. 2001). All indices are available at monthly mean resolution at the NOAA/ESRL/PSL website (<https://psl.noaa.gov/>). Annual mean indices are computed from monthly mean data, and a 10-yr fifth-order Butterworth low-pass filter is applied for smoothing purposes where relevant.

b. Hadley circulation strength

The HC can be described via the zonal-mean meridional streamfunction (ψ), computed as a vertical integral of the zonal-mean meridional wind (Peixoto and Oort 1992)

$$\psi(\phi, p) = \frac{2\pi R \cos\phi}{g} \int_0^p [v](\phi, p') dp', \quad (1)$$

where $[v]$ is the zonal- and annual/seasonal-mean meridional wind, R is Earth's radius, g is gravitational acceleration, ϕ is latitude, and p is pressure. Here we assume that $\psi = 0$ at the top of the atmosphere.

To account for the vertical and meridional inhomogeneities in the trends of the annual/seasonal-mean HC strength (see Figs. S1–S3 in the online supplemental material) and to encompass the trends in the strength of the overall HC, we use a metric of average HC strength [instead of the conventional 500-hPa ψ_{\max} ; see arguments in Pikovnik et al. (2021)]. For the NHC this yields

$$\langle \psi \rangle = \langle \psi(\phi, p) \rangle, \quad \text{for } \psi(\phi, p) > 0 \quad \text{and} \\ (\phi, p) \in [15^\circ\text{S}, 45^\circ\text{N}] \times [100, 1000] \text{ hPa}, \quad (2)$$

where ψ is uniformly sampled meridionally (every 1°) and vertically (every 50 hPa). An analogous measure is defined for the SHC, but with conditions of $\psi < 0$ and $\phi \in [45^\circ\text{S}, 20^\circ\text{N}]$. The metrics are thus data-adaptive averages and not simple box averages of ψ . Note that the SHC typically has a wider extent than the NHC; thus, the measure is then sampled to 20°N instead of 15°S, which would be equivalent to the NHC [Eq. (2)].

The linear trends $\Delta\psi/\Delta t$ are computed from the time series of ψ for each (ϕ, p) as regression coefficients. The same procedure is used to evaluate the trends $\Delta\langle\psi\rangle/\Delta t$ of the average HC strength. The trends are considered significant if they pass the 95% threshold of the modified Mann–Kendall test, using the trend-free prewhitening method (Yue and Wang 2002).

c. Kuo–Eliassen equation

In the atmosphere, the zonal-mean meridional circulation is maintained by diabatic heating, friction, and eddy heat and momentum fluxes. To analyze to what extent each of these processes contributes to the Hadley circulation and its changes we solve the Kuo–Eliassen (KE) equation for the mean meridional streamfunction ψ . We derive the *extended* KE equation without quasigeostrophic assumptions, which are generally not applicable to the deep tropical atmosphere, building on the previous work of Kim and Lee (2001) and Chemke and Polvani (2019, 2020). The extended KE equation is derived from the zonally averaged momentum, thermodynamic, continuity budgets, and the thermal wind equation, and therefore links the zonally averaged meridional circulation ψ with various forcings. The extended KE equation is an elliptic second-order partial differential equation (for details see appendix A):

$$L\psi = D_{Q_\phi} + D_{v'T'} + D_X + D_{w'v'} + D_{w'\omega'} + D_{\omega'\theta'}. \quad (3)$$

Forcing terms on the right-hand side (RHS) of Eq. (3) are

$$D_{Q_\phi} = \frac{R_d}{p} \frac{\partial [J]}{R \partial \phi}, \quad (4)$$

which represents meridional gradient of the zonal-mean diabatic heating $[J]$ [latent, sensible, and radiative, in K s^{-1} ; defined in Eq. (A11)];

$$D_X = -f \frac{\partial [F_\lambda]}{\partial p}, \quad (5)$$

which represents vertical gradient of the zonal-mean zonal friction $[F_\lambda]$ [defined in Eq. (A10)];

$$D_{v'T'} = -\frac{R_d}{p} \frac{\partial}{R \partial \phi} \frac{\partial [(v'T') \cos \phi]}{R \cos \phi \partial \phi}, \quad (6)$$

which includes the zonal-mean meridional eddy heat flux;

$$D_{wv'} = f \frac{\partial^2 [(u'v') \cos^2 \phi]}{R \cos^2 \phi \partial p \partial \phi}, \quad (7)$$

which includes the zonal-mean meridional eddy momentum flux;

$$D_{w\omega'} = f \frac{\partial^2 [u'\omega']}{\partial p^2}, \quad (8)$$

which includes the zonal-mean vertical eddy momentum flux; and

$$D_{\omega\theta'} = -\frac{1}{\rho[\theta]} \frac{\partial}{R \partial \phi} \frac{\partial [\omega'\theta']}{\partial p}, \quad (9)$$

which includes the zonal-mean vertical eddy heat flux. In Eqs. (4)–(9), R_d is the gas constant of dry air, p is pressure, $f = 2\Omega \sin \phi$ is the Coriolis parameter, ρ is density, and $[\theta]$ is zonal-mean potential temperature. Operator L in Eq. (3) is an elliptic second-order linear differential operator, which describes the structure of the zonal-mean state of the atmosphere, including static stability and spatial structure of the zonal-mean zonal wind.

The resulting streamfunction ψ^{KE} verifies well with the exact ψ [computed from Eq. (1)] across the meridional cross section, as shown in Fig. S4b. The solution of the extended KE equation ψ^{KE} also verifies somewhat better with the exact solution ψ [Eq. (1)] than the solution $\psi_{\text{OG}}^{\text{KE}}$ of the quasigeostrophic (QG) KE equation (Fig. S4a; see also Chemke and Polvani 2019). For the period 1979–2018 and the presented domain (Fig. S4), the mean absolute value of the difference $\Delta\psi^{\text{KE}} = \psi^{\text{KE}} - \psi$ is roughly 20% smaller than $\Delta\psi_{\text{OG}}^{\text{KE}} = \psi_{\text{OG}}^{\text{KE}} - \psi$ in ERA5 and 37% smaller in ERA-Interim.

The HC strength is obtained from ψ^{KE} and ψ by spatially averaging them over each Hadley cell [Eq. (2)]. The comparison of the time series of the HC strength $\langle \psi^{\text{KE}} \rangle$ and $\langle \psi \rangle$ reveals that the two time series are aligned (Fig. S5). The correlation between time series is also greater than 0.92 for both cells and reanalyses; accordingly, hereafter we only show the

results for the HC strength obtained from the Kuo–Eliassen equation $\langle \psi^{\text{KE}} \rangle$ (unless otherwise specified).

The contributions of different physical processes to the changes of the HC strength are evaluated based on the decomposition of Kim and Lee (2001) and Chemke and Polvani (2019). The linear operator in (3) is expanded as $L(t) = L_0 + \delta L(t)$, where L_0 denotes a reference operator (corresponding to year 1979) and $\delta L(t)$ the deviation therefrom. Similarly, the streamfunction solution is expanded as $\psi(t) = \psi_0 + \delta\psi(t)$, and the forcing terms as $D(t) = D_0 + \delta D(t)$. The decomposition allows us to describe the total change of the streamfunction, $\delta\psi$, by the partial changes $\delta\psi_j$ associated with the changes in physical forcing D_j , such that $L_0\delta\psi_j = \delta D_j$, and by the change $\delta\psi_{S^2}$, associated with the change of static stability S^2 , which is the main contributor to changes δL of the operator L . Here, j applies to the physical processes (4)–(9) (i.e., $j = Q_\phi, v'T', X, u'v', u'\omega', \omega'\theta'$). The details of the derivation are presented in appendix B.

3. Drivers of the Hadley circulation strength and its trends

An inspection of ERA5 suggests strengthening of the NHC (Fig. 1a) until ~2002, and a slow decline afterward, whereas the stronger SHC (Fig. 1b) shows a steady strengthening before ~2002 and a stagnation afterward. ERA-Interim shows significant strengthening of both HCs in the 2000s [consistent with Nguyen et al. (2013)], which has been attributed to data assimilation artifacts (D'Agostino and Lionello 2017). Overall, there are no significant trends in the strength of both annual-mean HCs in ERA-Interim (Figs. 1c,d) in the 1979–2018 period. On the contrary, the NHC in ERA5 strengthens significantly, mostly in spring [March–May (MAM)]. The SHC in ERA5 also strengthens significantly, mostly in austral spring/autumn. The strengthening of the NHC is in line with previous studies (Tanaka et al. 2004; Quan et al. 2004; Mitas and Clement 2005; Stachnik and Schumacher 2011), whereas the strengthening of the SHC in austral winter has been studied less as the indicated trends were generally weaker. Here we show that these trends can be as strong as for their Northern Hemisphere counterpart in ERA5.

By comparing the time series of the HC strength in ERA5 and ERA-Interim, we observe that the two reanalyses are better aligned at the interannual time-scale than at the decadal time scale. Indeed, the correlations of the time series, filtered by an 8-yr high-pass filter that captures ENSO variability, show high correlation ($r = 0.86$ for SHC and $r = 0.65$ for NHC) between the two reanalyses. On contrary, the correlations of the original time series, dominated by the decadal variability, are weak to moderate.

Since the differences between the two reanalyses can be significant on decadal and longer time scales, we first analyze the drivers of the HC strength. In section 4 we then extend this analysis to assess whether the HC strengthening in the recent decades is an artifact or a consequence of interannual–multi-decadal variability.

As described in the previous section, the Hadley circulation strength is affected by diabatic heating, stationary and

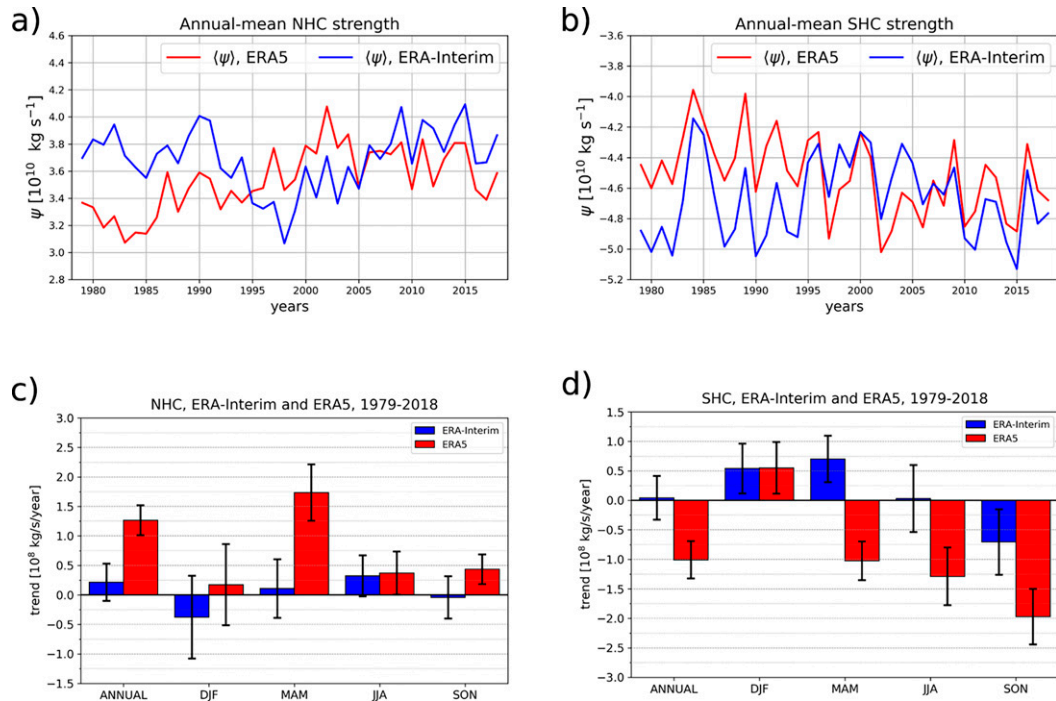


FIG. 1. The time evolution of the annual-mean average HC strength $\langle \psi \rangle$ following Eqs. (1) and (2) for (a) the NHC and (b) the SHC. Annual-mean and seasonal-mean linear trends (as labeled) for (c) the NHC and (d) the SHC. The error bars in (c) and (d) represent the 95% confidence interval. Note that the y axes in different panels are not the same. Note that increasingly negative values in (b) and negative values in (d) indicate intensification of the southern cell.

transient eddies via eddy heat and momentum fluxes, and by frictional processes (Vallis 2006). These processes represent forcing terms in the Kuo–Eliassen Eq. (3) and determine the resulting streamfunction field $\psi(\phi, p)$ for each year/season. The meridional cross sections of climatologies and trends of the RHS terms in the Kuo–Eliassen Eq. (3) are provided in Figs. S6 and S7, but are not discussed further, as we focus on their contributions, spatially averaged over the Hadley cell following Eq. (2).

Figure 2 shows time series of contributions of different physical processes to the variability of the Hadley cell strength $\langle \delta \psi \rangle$ between 1979 and 2018 for ERA5, and Fig. S8 shows the same for ERA-Interim. Figure 3 and Fig. S9 show their corresponding trends, whereas the correlations between the time series of the HC strength and time series of contributing processes are given in Table 1. The main driver of the HC strength changes and the main source of variability in the strength of the annual-mean HC is the meridional gradient of

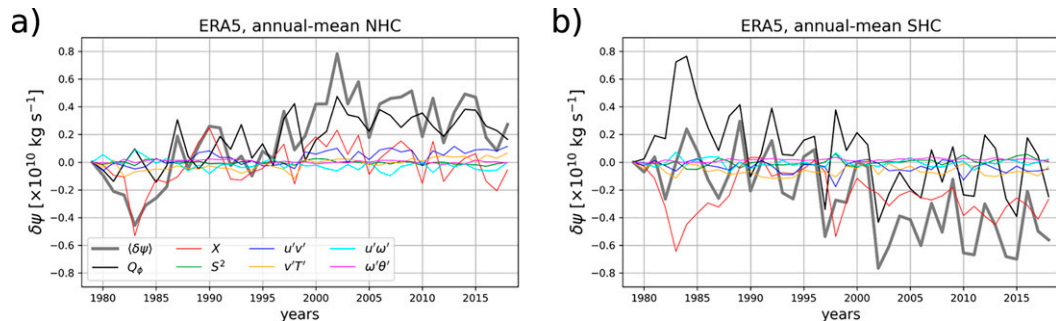


FIG. 2. Time series of (a) annual-mean NHC strength and (b) SHC strength in ERA5 from 1979 to 2018. Anomalies are computed relative to the reference year values (1979). Gray line denotes the total change of HC strength $\langle \delta \psi \rangle$ and different contributions to $\langle \delta \psi \rangle$ are denoted as follows: black line is meridional gradient of diabatic heating (Q_ϕ), red line is zonal friction (X), green line is static stability (S^2), blue line is meridional eddy momentum flux ($u'v'$), orange line is meridional eddy heat flux ($v'T'$), cyan line is vertical eddy momentum flux ($u'\omega'$), and purple line is vertical eddy heat flux ($\omega'\theta'$). Note that the negative values in (b) indicate intensification of the southern cell.

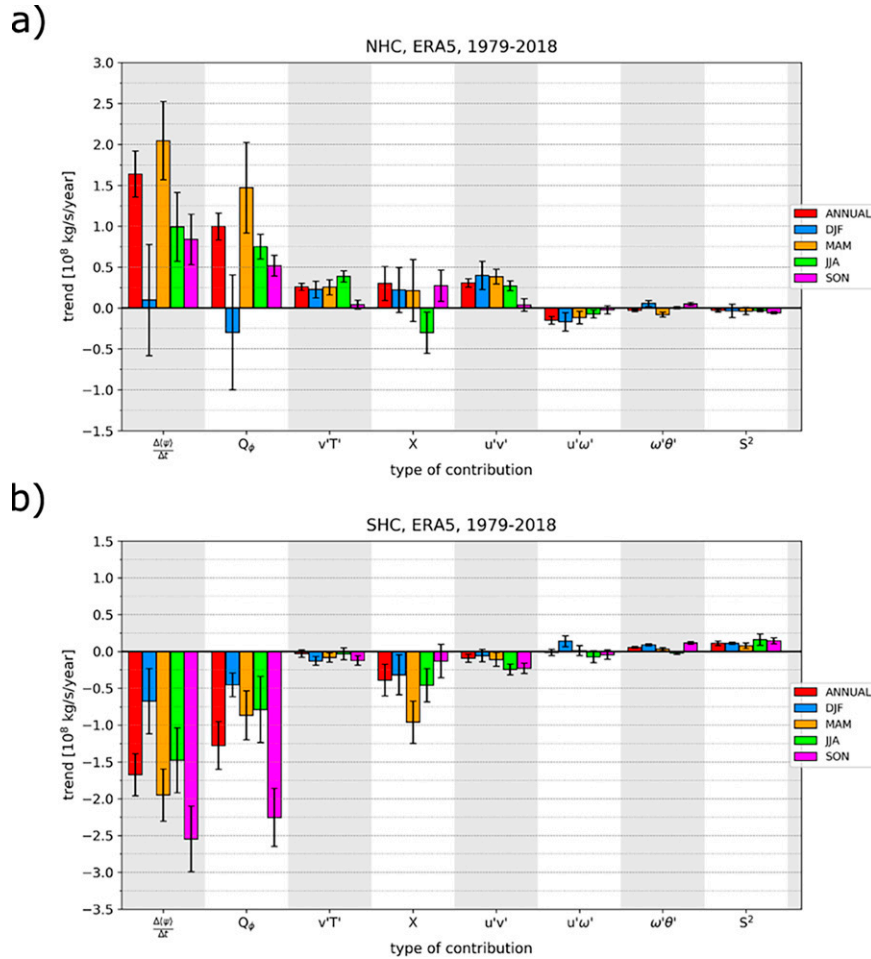


FIG. 3. Trends of the annual-mean and seasonal-mean (a) NHC and (b) SHC strength between 1979 and 2018 in ERA5. The first column, $\Delta(\psi)/\Delta t$, shows the total trend of HC strength. The remaining columns show contributions of the physical processes maintaining HC [Eq. (A7)] to the total trend: diabatic heating Q_ϕ , friction X , static stability S^2 , meridional eddy momentum fluxes $u'v'$, meridional eddy heat fluxes $v'T'$, vertical eddy momentum fluxes $u'\omega'$, and vertical eddy heat fluxes $\omega'\theta'$. Different colors (as labeled) represent different months, red color represents annual mean trends. The negative values in (b) indicate intensification of the southern cell.

diabatic heating Q_ϕ . This applies to both reanalyses and both HCs. On the contrary, friction X importantly modulates the Hadley circulation response to diabatic heating only in the NHC ($r = 0.76$ in ERA5 and $r = 0.84$ in ERA-Interim), particularly at the interannual time scale, whereas its impact on the SHC strength is limited (Table 1) both at decadal and interannual time scales (not shown). The two interconnected processes, diabatic heating and friction, can also explain the weakening of the NHC in ERA5 from ~ 2002 on (see Table 1 and Fig. 2).

The strengthening of the HC through the gradient of diabatic heating is largely associated with 1) enhanced latent heating in the tropics [observed also by Chemke and Polvani (2019)] and 2) enhanced diabatic (radiation) cooling in the subtropics (see Fig. 4b below and Fig. S6b); the converse is true for weakening. The first consideration (the strengthening effect of enhanced latent heating) can be explained by the

enhanced condensation rate due to (i) increased water vapor content in the tropical troposphere and (ii) the enhanced moisture convergence (Sohn and Park 2010), resulting from stronger trade winds and increased water vapor content in the lowest parts of the subtropical troposphere (not shown). The second (the strengthening effect of enhanced diabatic cooling) can be partly explained by the fact that an air parcel in a warmer subtropical atmosphere emits increasingly more radiation.

The strengthening of the HC through friction is associated with stronger trade winds, since in the lower part of the HC the frictional force on the zonal wind balances the Coriolis force on the meridional flow [see Eq. (A10)]. By approximating $[F_\lambda]$ as Rayleigh friction (i.e., $[F_\lambda] \approx -[u]/\tau$, with relaxation time scale τ), it can be shown that friction X is ultimately proportional to $-f[u]/\tau$. Therefore, stronger equatorial easterlies and zonal friction enhance the HC. Note that the equatorial

TABLE 1. Correlations of the annual-mean Hadley cell strength $\langle \delta\psi \rangle$ time series with the time series of their contributing physical processes (1979–2018): diabatic heating Q_ϕ , friction X , static stability S^2 , meridional eddy momentum fluxes $u'v'$, meridional eddy heat fluxes $v'T'$, vertical eddy momentum fluxes $u'\omega'$, and vertical eddy heat fluxes $\omega'\theta'$. Anomalies were computed relative to 1979. Only correlations exceeding the 95% significance threshold are shown.

	NHC ERA5	SHC ERA5	NHC ERA-Int	SHC ERA-Int
Q_ϕ	0.77	0.83	0.69	0.89
$v'T'$	0.57	—	—	0.32
X	0.76	—	0.84	—
$u'v'$	0.70	0.39	0.60	0.35
$u'\omega'$	−0.64	—	—	—
$\omega'\theta'$	—	−0.45	—	−0.36
S^2	—	−0.55	—	—

easterlies can be driven both by the diabatic heat sources as well as by the zonal SST gradients.

Extratropical eddy heat and momentum fluxes generally shape the dynamics of the midlatitudes as well as act to constrain the width and strength of the Hadley cell. For example, the extratropical eddies produce eddy momentum flux divergence in the subtropical upper troposphere (Figs. S6e and S7e) (Zurita-Gotor and Álvarez-Zapatero 2018), which contributes to the Hadley cell driving (Table 1). On the other hand, the tropical eddies produce eddy momentum flux divergence in the subtropics and convergence in the ITCZ (Zurita-Gotor 2019a,b). The eddy momentum flux divergence in the subtropics is increasing in both HCs and in both studied reanalyses in the 1979–2018 period (Figs. S6f and S7f), acting to enhance the Hadley circulation, while also being an important driver of the HC variability (Table 1) (as also suggested by Zurita-Gotor 2019a,b; Hoskins et al. 2020; Hoskins and Yang 2021). However, its impact on the long-term HC strength trends is much smaller than that of the diabatic and frictional processes. The impact of meridional eddy heat fluxes on the trends and variability of the HC strength is important only in

the NHC in ERA5, driven by the increase of eddy heat flux divergence in the NH subtropics (Fig. S6h).

Both reanalyses also show that the static stability slightly weakens the Hadley circulation in 1979–2018 period, with somewhat greater weakening in the winter hemisphere cell (in DJF for NHC, and JJA for SHC; Fig. 3 and Fig. S9). The result is also in contrast to some other studies (e.g., Mitas and Clement 2006), which argued that reduced static stability can explain an intensification of the Hadley circulation already in the historical period. Note that our result merely means that in the analyzed historical period S^2 is not the main driver of the HC strength trends. However, the HC weakening by the end of the twenty-first century can nevertheless be explained by S^2 changes as proposed by Chemke and Polvani (2020) based on the analysis of the CMIP5 multimodel ensemble under abrupt $4 \times \text{CO}_2$ forcing.

The impact of other processes on the Hadley circulation changes is even smaller: $u'\omega'$ and $\omega'\theta'$ both act to weaken the circulation. Despite having a negligible impact in the 1979–2018 period, these processes might become more important contributors to the changes of the HC strength in the future, similar to the static stability (mentioned above). Furthermore, these mechanisms may be important for the local HC forcing or for the processes on much shorter time scales.

4. Hadley circulation trends or long-term variability?

a. Comparison with observed precipitation

The term Q_ϕ is the main driver of the HC strength $\langle \delta\psi \rangle$ in both hemispheres (Figs. 2 and 3). As previous studies (e.g., Chemke and Polvani 2019) suggested that most reanalyses exhibited unrealistic Q_ϕ , we now test it using observed precipitation as a proxy for latent heating. First, we test how much of the diabatic heating is explained by the latent heating. For example, Chemke and Polvani (2019, their Fig. 2c) showed that latent heating has a major impact on the HC strength trends in modern reanalyses, whereas radiative heating only has a marginal impact. As the latent heating

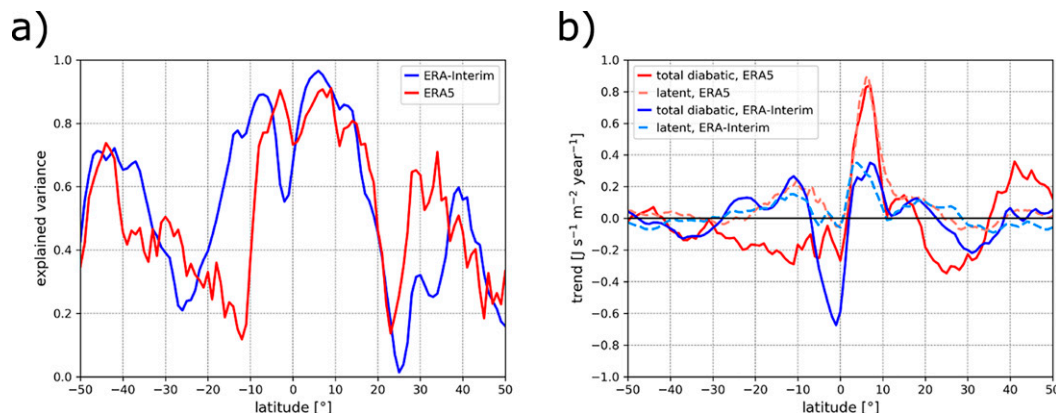


FIG. 4. (a) Variance of the annual-mean total diabatic heating explained by latent heating and (b) trends of the annual-mean total diabatic heating (solid line) and latent heating (dashed line) in ERA5 and ERA-Interim for the 1979–2018 period. Both latent heating and total diabatic heating are computed as tropospheric-column integrals of respective zonal-mean values.

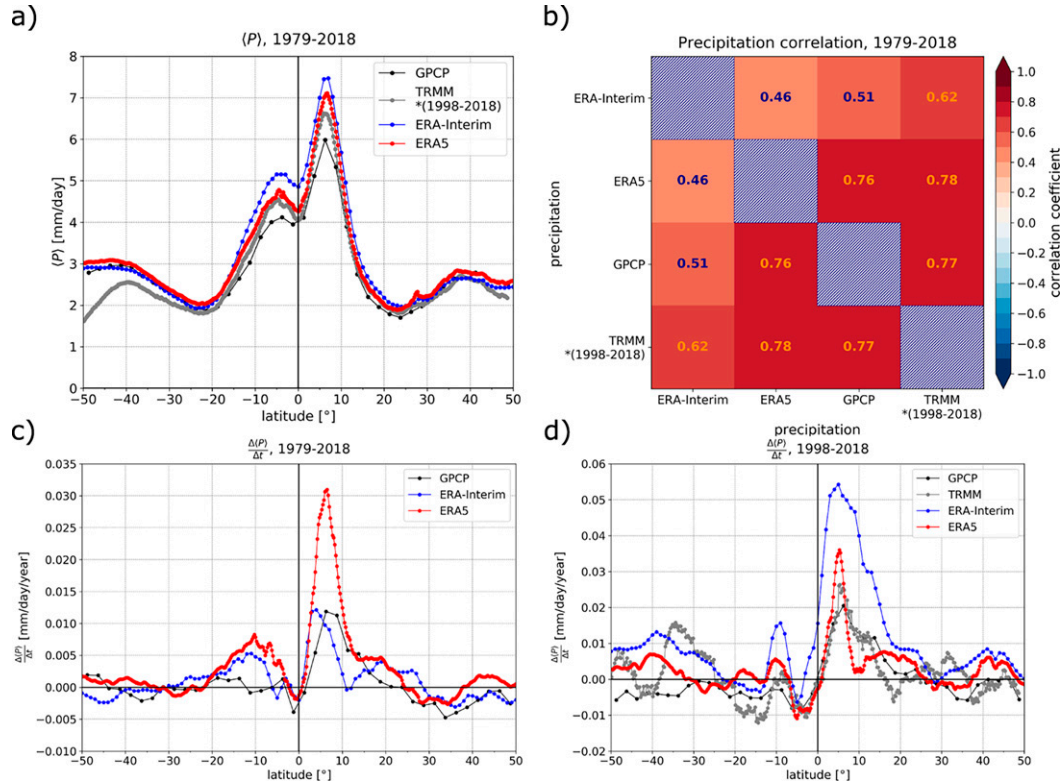


FIG. 5. (a) Climatological zonal-mean precipitation for ERA5 (red line), ERA-Interim (blue line), GPCP (black line), and TRMM (gray line). (b) Correlation of meridionally averaged precipitation (between 10°S and 10°N) between different precipitation datasets (as labeled). Zonal-mean precipitation trend (c) between 1979 and 2018 and (d) between 1998 and 2018. Note that the scales differ in (c) and (d).

and other diabatic heating sources are not available as an output variable in ERA5 and ERA-Interim, we compare tropospheric-column-integrated zonal-mean diabatic heating, $[Q^{\text{diab}}](\phi) = \int_{1000\text{hPa}}^{100\text{hPa}} [J](\phi, p) c_p (-dp/g)$ (unit: $\text{J s}^{-1} \text{m}^{-2}$), with precipitation-based proxy for column-integrated latent heating $[Q^{\text{lat}}](\phi) = L[P](\phi)$, where $L = 2.5 \text{ MJ kg}^{-1}$ represents the latent heat of condensation, c_p is specific heat at constant pressure for dry air, and $[P](\phi)$ is zonal-mean precipitation (unit: $\text{kg s}^{-1} \text{m}^{-2}$). The zonal-mean diabatic heating rate $[J](\phi, p)$ is evaluated as a thermodynamic residual using Eq. (A11).

In the tropics between 10°S and 20°N, 65%–95% of the variance of the diabatic heating is explained by latent heating (Fig. 4a). The explained variance is low in the subtropics, where radiation cooling dominates, and increases to 0.4–0.7 at around 30°–35°N/S, near the descending HC branch. In both ERA5 and ERA-Interim, most of the trend in the diabatic heating in deep tropics (ITCZ) is explained by the trend in latent heating (Fig. 4b), which is directly associated with the precipitation trend (Fig. 5c). In ERA-Interim, there is a clear negative trend in the diabatic heating in the SH tropics (also seen in Fig. S7b).

Given that the diabatic processes (Q_ϕ) are the main contributor to the trends in global HC strength $\langle \delta\psi \rangle$ and that these are obtained by taking a meridional and vertical average of $\delta\psi$ and $\delta\psi_{Q_\phi}$ following Eq. (2), we compare them to

the time series of the mean meridional gradient of the zonal-mean total diabatic heating (Q^{diab}). The mean meridional gradient is taken over the same meridional region as used for averaging to define HC strength [Eq. (2)]. Mathematically, the mean meridional gradient of the total diabatic heating reduces to the difference between the diabatic heating at the edges of a single HC, divided by their distance:

$$\begin{aligned} Q_\phi^{\text{diab}}(\text{NHC}) &= \left\langle \frac{\partial [Q^{\text{diab}}]}{R \partial \phi} \right\rangle (\text{NHC}) \\ &= \frac{[Q^{\text{diab}}](\phi_N) - [Q^{\text{diab}}](\phi_0)}{R(\phi_N - \phi_0)}, \\ Q_\phi^{\text{diab}}(\text{SHC}) &= \left\langle \frac{\partial [Q^{\text{diab}}]}{R \partial \phi} \right\rangle (\text{SHC}) \\ &= \frac{[Q^{\text{diab}}](\phi_0) - [Q^{\text{diab}}](\phi_S)}{R(\phi_0 - \phi_S)}, \end{aligned} \quad (10)$$

where ϕ_S denotes the southern boundary of the SHC, ϕ_N indicates the northern boundary of the NHC, and ϕ_0 marks their intersection. These boundaries are computed by vertically averaging meridional HC boundaries at pressure levels between 200 and

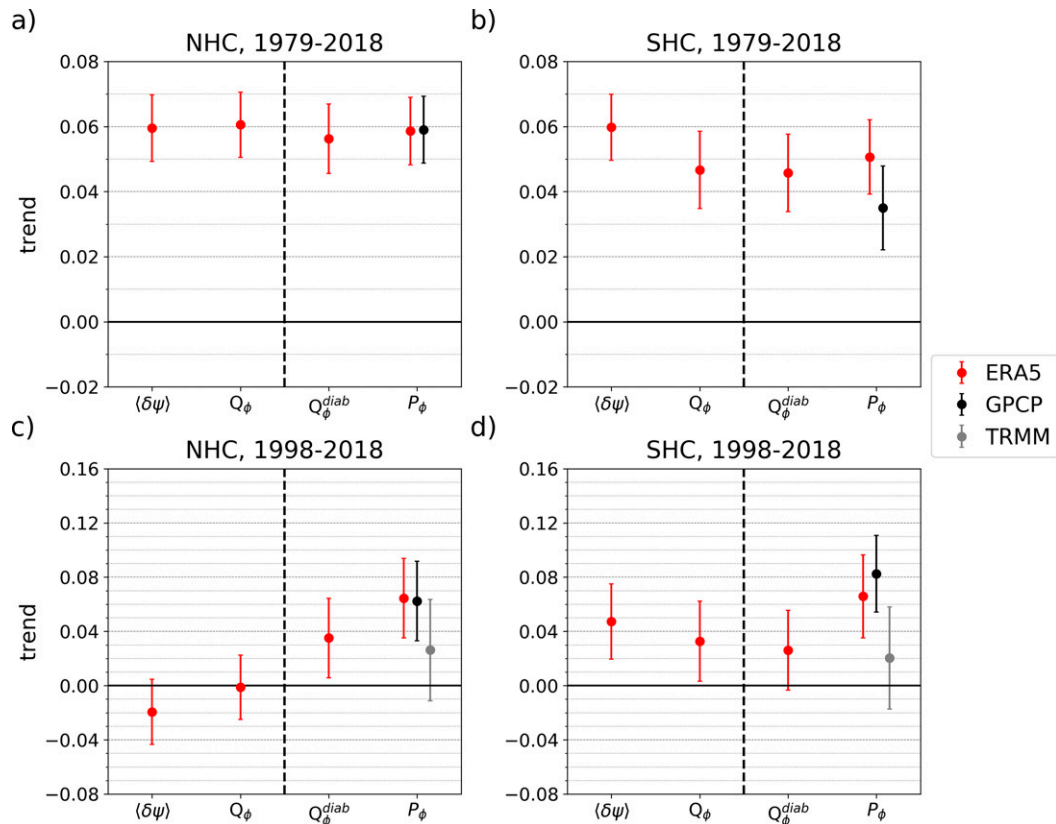


FIG. 6. Comparison of the trends of standardized time series. Hadley cell strength change $\langle \delta\psi \rangle$ and contribution of diabatic heating to the change of HC strength Q_ϕ are from ERA5. They are compared to the mean meridional gradient of total diabatic heating Q_ϕ^{diab} and precipitation $P_\phi = \langle \partial P \rangle / R \partial \phi$ in ERA5, GPCP, and TRMM for the (a),(c) NHC and (b),(d) SHC in two time periods: (a),(b) 1979–2018 and (c),(d) 1998–2018. The ψ values for SHC are multiplied by (-1) , and thus their positive trends suggest HC strengthening. For similar reasons, meridional precipitation gradients in the NHC are also multiplied by -1 .

900 hPa with a step of 50 hPa. This decreases the sensitivity of the diagnosed HC boundary to the vertical structure of the HC (Nguyen et al. 2013; Kang et al. 2013; D’Agostino and Lionello 2017). The term $[Q_\phi^{diab}](\phi)$ is then obtained by further averaging the tropospheric-column-integrated total diabatic heating in the 5° -wide symmetric latitudinal band centered around ϕ .

Trends of standardized time series (i.e., time series divided by their standard deviation) are compared in Fig. 6 for ERA5 and Fig. S10 for ERA-Interim, and their correlations are shown in Fig. 7. In the 1979–2018 period (Figs. 6a,b), the trends in the mean meridional gradient of the total diabatic heating Q_ϕ^{diab} are consistent with trends in $\langle \delta\psi \rangle$ and Q_ϕ for both cells in ERA5. Their sign is also in line with the sign of trends in the mean meridional gradient of precipitation $P_\phi = \langle \partial P \rangle / (R \partial \phi)$ in ERA5 and GPCP, which is computed analogously as Q_ϕ^{diab} in Eq. (10). During the 1998–2018 period, for which TRMM data are also available, the trends of the SHC strength are compatible with the trends of Q_ϕ^{diab} , and with the trends of P_ϕ for TRMM, as well as (within the margin of error) with the trends of P_ϕ for GPCP and ERA5 (Fig. 6d). However, for the NHC in ERA5, the strengthening of the diabatic heating gradient and precipitation gradient does

not match the weakening of the NHC (Fig. 6c). Despite opposing trends between the NHC strength, and diabatic heating and precipitation gradient during 1998–2018, the correlations between these quantities remain moderate over the whole 1979–2018 period (Fig. 7; e.g., 0.69 for $\langle \delta\psi \rangle$ and 0.60 for Q_ϕ correlations with GPCP, and similarly with ERA5 precipitation data). The correlations are higher in the SHC (e.g., 0.64 for $\langle \delta\psi \rangle$ and 0.75 for Q_ϕ correlations with GPCP, and even higher with ERA5 precipitation data). On the other hand, the TRMM dataset shows no statistically significant correlations with either ERA5 or ERA-Interim HC strength.

ERA-Interim HCs generally exhibit trends that have the same sign as the precipitation gradient (Fig. S10). However, this is not true for the trend of Q_ϕ^{diab} in the SHC (Figs. S10b,d), which is opposite to the trends of the HC strength and its main contributor Q_ϕ . This anomaly has been also identified in Fig. 4b. On the other hand, the ERA-Interim HC strength correlates well with the precipitation gradient only in the Southern Hemisphere, whereas there is a poor verification of the ERA-Interim HC strength with the precipitation gradients in the Northern Hemisphere, consistent with, for example, Chemke and Polvani (2019). Comparing Fig. 2 and Fig.

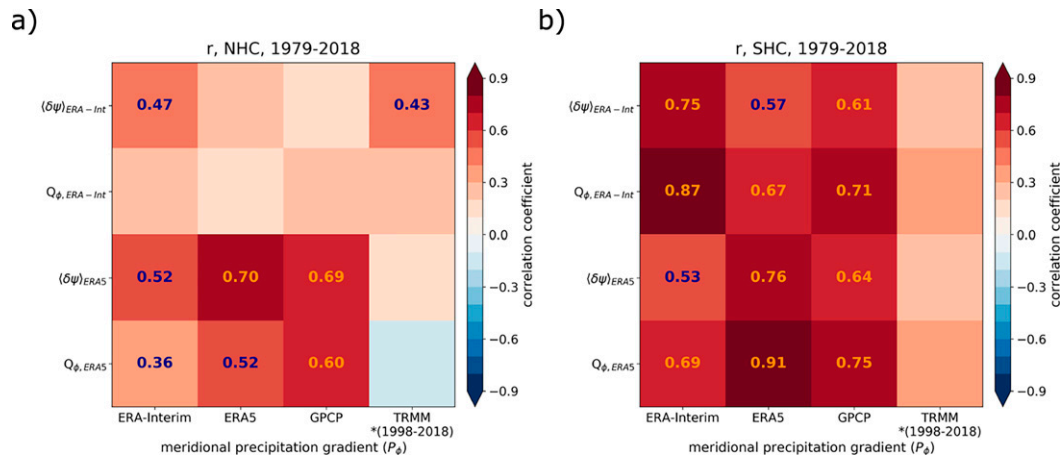


FIG. 7. Correlation between the strength of the Hadley cell ($\langle \delta\psi \rangle$) in ERA-Interim and ERA5, the contribution of meridional gradient of the diabatic heating to the HC strength (Q_{ϕ}) in ERA-Interim and ERA5, and the mean meridional precipitation gradient (P_{ϕ}) in ERA-Interim, ERA5, GPCP and TRMM data, for (a) NHC and (b) SHC. Only correlations exceeding the 95% significance threshold are shown.

S8 one can also notice a very different HC strength variability between the two reanalyses, which is likely the cause of the overall weaker correlations in ERA-Interim compared with ERA5.

Despite the fact that the above analysis suggests that the changes in precipitation can in general verify with the trends in the HC strength, caution is needed. The ERA-Interim mean precipitation shows large biases against both GPCP and TRMM observations, much larger than ERA5 (Fig. 5a; see also Fig. S11). This applies both to the whole tropical band as well as to the land-only areas (Fig. S11b), where GPCP makes use of relatively more accurate rain gauge precipitation measurements via GPCC. ERA-Interim tends to exaggerate deep convection and moisture influx in the tropics, resulting in excessive precipitation (Nogueira 2020), and this large bias makes it somewhat less reliable for the estimation of trends. Compared to ERA-Interim, ERA5 largely reduces biases in the dynamical fields (Hersbach et al. 2020), which makes it particularly useful to estimate the changes in the general circulation (Simmons 2022).

However, over the 1979–2018 period, ERA5 greatly overestimates the precipitation trend in the ITCZ ($0.031 \text{ mm day}^{-1} \text{ yr}^{-1}$) against GPCP ($0.012 \text{ mm day}^{-1} \text{ yr}^{-1}$; Fig. 5c), whereas it verifies well with the trends in TRMM and GPCP in the shorter 1998–2018 time period (Fig. 5d). On the other hand, ERA-Interim precipitation trends in the tropics deviate by a large margin from GPCP and TRMM in 1998–2018, but seemingly aligns well with GPCP over the longer 1979–2018 period. However, an inspection of time series reveals that the 1979–2018 precipitation trend in ERA-Interim is artificial, as it is only a combination of a slightly decreasing trend until 2000 and an increasing trend afterward, while none of them separately verifies with GPCP (Fig. S11). An overall better verification of the ERA5 tropical precipitation compared with ERA-Interim is further emphasized by its correlations with GPCP (Fig. 5b).

While identifying the source of the bias in the ITCZ precipitation trend in ERA5 is beyond the scope of this study, it appears that the difference in the zonal-mean tropical precipitation between ERA5 and GPCP suddenly increases in the early 2000s (Fig. S11a). The source of this difference is certainly not land areas as ERA5 verifies with GPCC and GPCP (which uses GPCC) even better lately (Fig. S11b). This means that the growing difference in precipitation between ERA5 and GPCP originates from the satellite-observed precipitation over ocean areas. Indeed, ERA5 started assimilating a plethora of new instruments between 2000 and 2004, mainly the geostationary radiances and microwave sounders (see Hersbach et al. 2020, their Figs. 4 and 5), which both affect precipitation. On the other hand, the reanalysis fit to observations is improving with time, allowing more trust in the latest reanalysis data (Hersbach et al. 2020, their Figs. 1, 12, and 14).

Note that a possible reason for the differences in rainfall trends between GPCP and ERA5 is that GPCP underestimates precipitation response to (increasing) SSTs, as was recently found by comparing GPCP data to the Global Tropical Moored Buoy Array data (Good et al. 2020). Based on this and the above results, we can conclude that the ERA5 precipitation trend likely somewhat overestimates the true precipitation trend in the tropics. The true precipitation trend is increasing as well, as seen from GPCP and TRMM data.

Altogether, the comparison of the HC strength trends and variability with precipitation data suggests that the increasing HC trend in ERA5 reanalysis during 1979–2018 is likely partly physical and partly an artifact of misrepresentation of the latent heating in this reanalysis. As global warming studies (e.g., Chemke and Polvani 2019, 2020) have shown that the HC would weaken by the end of the twenty-first century, we explore below the interannual-to-multidecadal variability as a possible (physical) mechanism for the recent strengthening of the HC.

Table 2. Correlations of different northern and southern HC-related time series with different decadal-to-multidecadal indices (as labeled). Time series were first filtered using 10-yr low-pass Butterworth filter. Maximum correlation is provided at a specified lag in years (in parentheses), assessed within ± 15 years. Alternative correlations are shown in square brackets where relevant. At negative lags the index leads. Only values that are significant at the 95% level (based on a two-tailed t test) are shown. Annual mean data for 1950–2018 from ERA5 are used [except for precipitation (1979–2018)], since GPCP is available only from 1979 onward; lag correlations are then only explored within a ± 5 -yr window). $\langle \psi \rangle$ denotes HC strength, Q_ϕ is diabatic heating contribution to HC strength, and X indicates contribution from friction, where the time series are multiplied by -1 for the SH cell for easier comparison with the NH cell. Precipitation time series (GPCP and ERA5) are averaged within the tropical belt (15°S – 15°N). U850 (NH) denotes mean zonal wind at 850 hPa between 5° and 20°N , whereas U850 (SH) denotes the 5°S – 5°N average.

Time series	AMO (lag)	IPO (lag)	PDO (lag)
$\langle \delta\psi \rangle$ (NH)	0.77 (−3) [0.73 (0)]	−0.47 (−1) [0.56 (−9)]	0.69 (−15) [−0.49 (+6)]
$-\langle \delta\psi \rangle$ (SH)	0.85 (+3) [0.80 (0)]	0.51 (−15)	0.67 (−15) [−0.43 (+15)]
Q_ϕ (NH)	0.77 (+9) [0.55 (0)]	0.49 (−10) [−0.40 (+3)]	0.72 (−15)
$-Q_\phi$ (SH)	0.80 (+3) [0.75 (0)]	0.68 (−12) [−0.48 (−3)]	0.66 (−15) [−0.53 (+15)]
ERA5-prec.	0.96 (−2) [0.94 (0)]	−0.72 (−2) [−0.69 (0)]	−0.74 (−5) [−0.53 (0)]
GPCP-prec.	0.75 (−5) [0.50 (0)]	−0.73 (−5) [−0.56 (+4)]	−0.86 (−5) [−0.58 (+5)]
X (NH)	0.66 (−3) [0.59 (0)]	−0.79 (+10) [0.63 (−10)]	0.66 (−15) [−0.60 (+9)]
$-X$ (SH)	0.49 (+14) [0.46 (0)]	−0.35 (−11) [0.30 (+10)]	0.39 (0)
U850 (NH)	−0.66 (+3) [−0.60 (0)]	0.52 (0) [−0.44 (−7)]	−0.67 (−15)
U850 (SH)	−0.71 (+2) [−0.66]	−0.64 (−15) [0.47 (+11)]	−0.69 (−15) [0.45 (+11)]

b. Comparison with interannual-to-multidecadal variability

Variability in the strength of both HCs in ERA5 is now compared to the leading modes of interannual-to-multidecadal SST variability (Table 2, Fig. 8; see also Fig. S12). Since the period of these phenomena is up to 70 years, the ERA5 back-extension data for 1950–78 are additionally used in the comparison, and the time series of the HC strength in other long-range modern reanalyses (ERA-Interim, ERA-20C, CERA-20C, NOAA-20CR, NCEP) are analyzed as well. Note that the aim of this section is to identify *potential* relationships (covariability and potential lead-lag relationships) between the HCs and the decadal–multidecadal indices, which should be explored in more detail in the future.

Figure 8a shows that the SHC strength in all reanalyses exhibits strengthening in the last four decades. It is also evident that the SHC strength derived from different reanalyses generally closely follows the AMO (red solid line) throughout the analyzed period, with the exception of CERA-20C and ERA-Interim. ERA-Interim is likely too short for comparison with the decadal-to-multidecadal indices, although it is also less reliable than, say, ERA5 due to the arguments presented

in the previous sections. CERA-20C is a coupled atmosphere–ocean reanalysis. Thus, the potential biases in the atmospheric observations immediately impact the state of the ocean. As such, it is also less suitable for the comparison of its interannual-to-multidecadal variability with the leading oceanic modes of variability.

HC strength deduced from NOAA-20CR and ERA-20C reanalyses closely aligns with the AMO also over longer time periods. Both reanalyses assimilate only surface observations of atmospheric pressure (ERA-20C also includes marine surface winds), while they are forced by prescribed SST and sea ice distribution, meaning that these reanalyses can capture the leading modes of the SST variability, which affect the atmospheric circulation. Furthermore, the AMO index is also closely followed by the HC strength in ERA5 and NCEP reanalyses. SHC indeed shows high correlations with the AMO across different reanalyses (although lags differ slightly; Fig. S13a). The correlations of the SSTs and the SHC strength show that the SHC strength signal mainly originates from the North Atlantic, further confirming the role of the AMO (Fig. 9a).

On the other hand, the NHC strength in different reanalyses shows different behavior (Fig. 8b). There are increasing

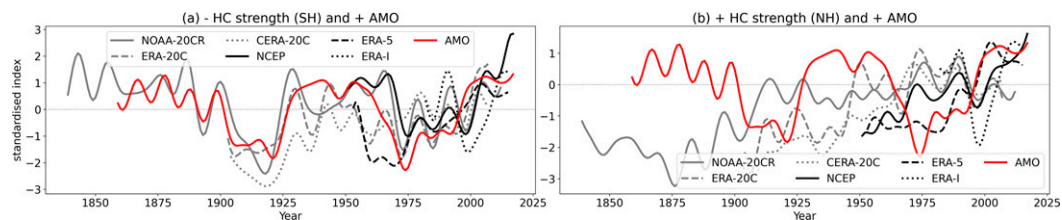


FIG. 8. Comparison of Hadley cell strengths across six different reanalyses (as labeled) and the AMO index for the (a) SHC and (b) NHC. Note that here we use HC strength measure defined in Eqs. (1) and (2), and that all time series are standardized (divided by standard deviation). Time series of SHC strength in (a) were multiplied by -1 for easier comparison with AMO. All time series were filtered using a 10-yr low-pass Butterworth filter, and the first and last 3 years of the time series are excluded due to filtering.

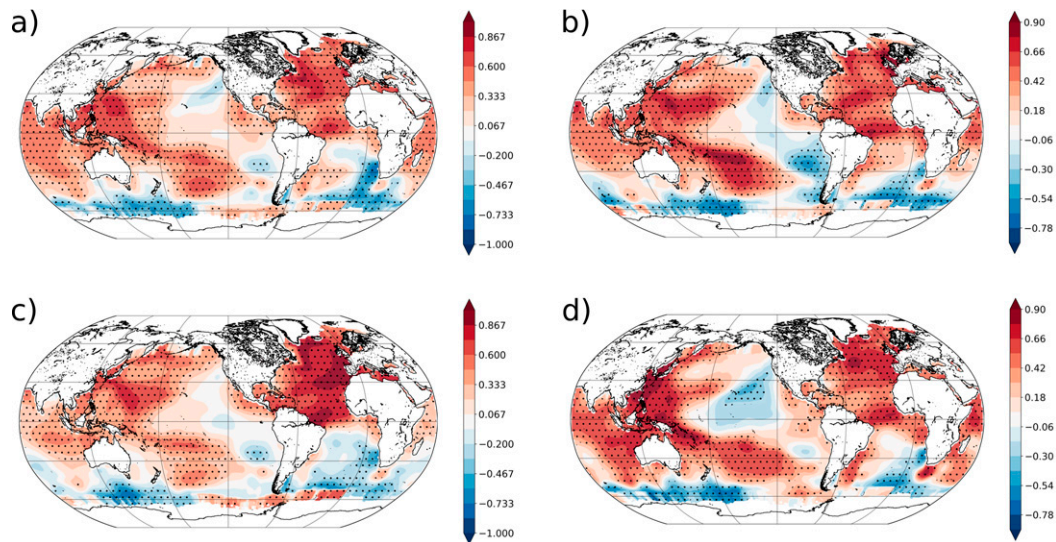


FIG. 9. Correlations of SSTs and (a) SHC strength in ERA5, (b) NHC strength in ERA5, (c) the AMO, and (d) the PDO for the 1950–2018 period. In (a)–(c) correlations at lag 0 years are shown, whereas in (d) correlations at lag 16 years are shown (i.e., provided SST pattern leads PDO by 16 years). Stippling denotes statistically significant correlations (at the 95% level). Data were first filtered with a 10-yr low-pass filter and SSTs were detrended with a long-term (1870–2018) linear trend (to be consistent with the AMO, IPO, and PDO indices). Last, a 10° spatial box averaging was performed.

trends in ERA-20C, CERA-20C, NCEP, and ERA5, and no trend in ERA-Interim; in NOAA-20CR there is a trend between 1875 and 1915, but it is largely steady afterward. Note that the NHC evolution in ERA5 largely follows the AMO; however, other reanalyses have a very different evolution, not consistent with the AMO. The larger differences between the AMO and the NHC strength in, for example, ERA-20C and NOAA-20CR, which are forced mainly by the SSTs, can be perhaps explained by the relatively smaller proportion of the ocean areas in the Northern Hemisphere through which the oceanic modes can influence the zonal-mean atmospheric circulation. The correlations of the NHC in different reanalyses with the AMO confirm that the link between the NHC and the AMO is only evident in ERA5 (Fig. S13b). The AMO-type signal can also be found in the correlation map between the SST and the NHC strength, but note that the impact of the Pacific SSTs on the NHC strength is relatively greater than for the SHC (Fig. 9b).

A strong relationship between the AMO and the strength of both HCs in ERA5 is also reflected in high correlations between the time series (Table 2 for 10-yr low-pass filtered data) in the 1950–2018 period: $r = 0.77$ for the NHC and $r = 0.85$ for the SHC. The warm phase of the AMO (AMO+) coincides with an enhanced meridional gradient of diabatic heating Q_ϕ ($r = 0.77$) in the Northern Hemisphere (NH) as well as in the Southern Hemisphere (SH; $r = 0.80$). The diabatic heating and its gradient are dominated by the latent heating (Fig. 4), whose proxy is precipitation (section 4a). Thus, the AMO also shows a high correlation with tropical precipitation in ERA5 ($r = 0.96$), albeit on a shorter (1979–2018) interval, as the GPCP data are only available from 1979 on.

Such a high correlation is consistent with Levine et al. (2018), who found that AMO+ is associated with significant precipitation increase in the Northern Hemisphere ITCZ. However, the AMO index shows a somewhat lower correlation with tropical precipitation in GPCP ($r = 0.75$), possibly due to GPCP's underestimation of precipitation response above oceans to increasing SSTs (Good et al. 2020).

A moderate correlation (Table 2) is also found between the AMO and the contribution of friction to the NHC strength (X). This could be related to stronger HC under AMO+, which is generally associated with stronger Walker circulation and stronger equatorial easterlies. Indeed, the correlation between the HC strength and the $[u]$ wind at 850 hPa is high, implying a relationship between the equatorial easterlies and the global HC strength. Furthermore, the correlation between the AMO and $[u]$ at 850 hPa is high as well, implying stronger (weaker) easterlies during AMO1 (AMO2) (see Table 2). As also established in section 3, X is proportional to $\pm([u]/\tau)$ in the NH/SH, respectively. This implies that also frictional processes, which affect the HC strength through equatorial easterlies and trade winds, can be impacted by the AMO.

How does the AMO+ (AMO-) strengthen (weaken) the Hadley circulation? Based on our analysis, the analysis of Li et al. (2016), and other studies mentioned below, we suggest the following mechanism (Fig. 10):

- 1) AMO has a tripole SST structure, where SST anomalies have the same sign in the tropics and midlatitude regions and an opposite sign in the subtropical regions (Krishnamurthy and Krishnamurthy 2016; Frajka-Williams et al. 2017). AMO+ means positive SST anomalies in the tropics and weaker positive (or slightly negative) SST

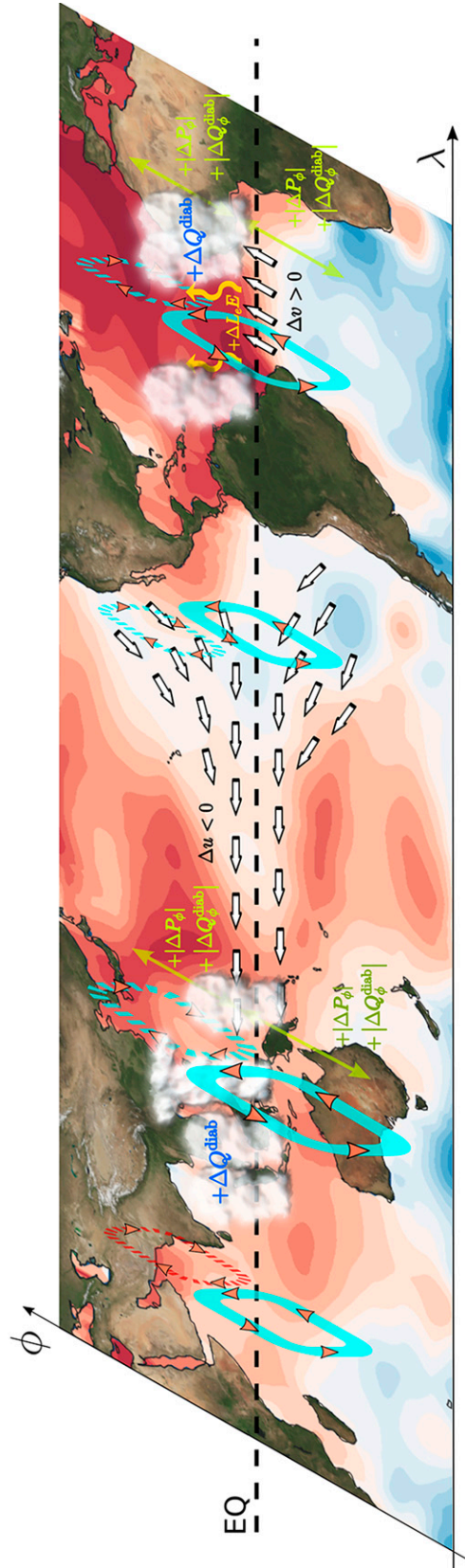


FIG. 10. Hadley circulation response to the warm AMO phase (AMO+). Contours represent SST anomaly correlation with AMO+ (Fig. 9c). The warm SST anomaly in the tropical North Atlantic increases latent heat flux ($+\Delta L_e E$) into the atmosphere, enhances the diabatic heating rate ($+\Delta Q^{\text{diab}}$), and strengthens the cross-equatorial flow in the lower branch of the Atlantic HC ($\Delta u > 0$). This is the direct Hadley circulation response to AMO, which only explains a minor part of the HC variability (Fig. S14). The dominant driver is the remote Indo-Pacific response, which includes an enhancement of equatorial easterlies in the Indian Ocean and west Pacific (Li et al. 2016). This initiates an enhanced diabatic heating over the Maritime Continent and through Bjerknes feedback leads to even stronger basinwide easterlies ($\Delta u < 0$) and Walker circulation (not shown) in the equatorial Pacific. White arrows indicate wind anomalies. Yellow-green two-way arrows represent enhanced meridional gradient of diabatic heating Q^{diab} and precipitation P_ϕ . Cyan cells represent strengthening local Hadley cells, whereas red cells represent weakening cells (Figs. S15 and S16). The thickness of the cell represents its strength (Fig. S17). Northern cells are dashed, as there is lesser consensus on the northern HC response to AMO. For detailed description of the mechanisms see text.

anomalies in the northern subtropical Atlantic (see also the schematic in Fig. 10). The positive SST anomaly in the tropics induces greater evaporation; that is, there is a net positive latent heat flux $+\Delta L_e E$ (E is evaporation rate, L_e is the specific latent heat of evaporation) from the tropical ocean into the atmosphere (Levine et al. 2018). More moisture results in greater precipitation and associated condensation heating, which scales roughly exponentially with column atmospheric water vapor. This further scales by the saturation specific humidity of the tropical ocean SST (He et al. 2018; Good et al. 2020). AMO+ also shifts the ITCZ northward and triggers strengthened flow toward the ITCZ (Levine et al. 2018), including stronger northward cross-equatorial flow in the lower troposphere (Green et al. 2017). Note that the global warming can further amplify the northward cross-equatorial flow by enhanced warming of the Northern Hemisphere compared to the Southern Hemisphere by which the ITCZ moves northward (Levine et al. 2018). Localized tropical diabatic heating in the Atlantic basin enhances meridional gradients of diabatic heating, (Q_ϕ) and precipitation (P_ϕ) between the ascending HC branch in the ITCZ and the descending branch in the subtropics, strengthening the HC (consistent with section 4a), as depicted in Fig. 10. However, the local Atlantic HC explains only a minor part of the global HC variability (0.1 for NHC, 0.07 for SHC; for ERA5, the period 1950–2018). Instead, the global HC variability is dominated by the Pacific HC (Fig. S14), although the data may be too short for definite conclusions. Thus, the local effect is likely limited and the remote effect of the AMO is dominant (see the next point).

- 2) Warm SST anomalies in the northern tropical Atlantic induce an enhanced interbasin SST gradient (e.g., Zhang and Delworth 2007), leading to an enhanced atmospheric temperature gradient. This induces easterlies in the Indian Ocean and western Pacific, and westerlies in the eastern Pacific, as shown in Li et al. (2016, their Fig. 3a). The easterlies in the western equatorial Pacific ultimately induce secondary deep convection over the Maritime Continent (Fig. 10, see also Green et al. 2017). This mechanism, amplified by the Bjerknes feedback and associated cooling of the eastern Pacific, induces easterlies over the whole equatorial Pacific (La Niña-like state) and enhances the Walker circulation (Hu and Fedorov 2018; Li et al. 2016, their Fig. 3b). Accounting for the high correlation between the U850 and HC strength (discussed above), this results in stronger trade winds and the strengthening of the Hadley circulation in the Pacific and Indian Oceans (Figs. S14–S16). However, the teleconnections between the Pacific and the Atlantic are complex, and thus other mechanisms could also be contributing to the links between the two ocean basins during different phases of the AMO.

On the interannual time scales, we compare the unfiltered HC strength variability with the Niño-3.4 index of ENSO. We find *small* negative correlation of the NHC strength with the Niño-3.4 index, whereas the correlation is positive for the

SHC strength, in contrast to some other studies (e.g., Nguyen et al. 2013; D'Agostino and Lionello 2017). This means that the SHC intensifies during the warm ENSO phase (El Niño) and weakens during the cold ENSO phase (La Niña). These results are consistent with Zhou et al. (2020), who studied the HC–SST coupling and found that warm equatorial eastern Pacific SSTs (El Niño) work to intensify the SHC but weaken the NHC.

While ENSO shows weak correlations with the HC strength, we find moderate correlations of the HC strength with other indices in the Pacific (IPO and PDO) that represent decadal-to-multidecadal variability (Table 2) and are often referred to as long-term variations of ENSO (their correlations with Niño-3.4 are 0.89 and 0.62, respectively; Table S1; see also Zhang et al. 1997). In particular, we find that PDO+ leads the HC strength by 15 years ($r = 0.69$ for NHC and 0.67 for SHC, Fig. 9d), and the HC strength leads PDO– by 5–15 years. This is consistent with the typical delay between the PDO/IPO and AMO (d'Orgeville and Peltier 2007).

This again suggests that the multidecadal variability of the coupled ocean–atmosphere system in the Pacific and Atlantic is likely strongly linked (see also Wang 2006; Zhang and Delworth 2007; McGregor et al. 2014; Li et al. 2016) and driving long-term variability in the HC strength. Consistent with the link between the AMO, HC strength, and the Pacific variability (IPO, PDO) are also correlations of PDO and IPO with Q_ϕ and precipitation (PDO+/IPO+ lead Q_ϕ by 10–15 years). Similarly, correlations of IPO and PDO with X and $[u]$ at 850 hPa are moderate to strong and act in the same way as for the AMO: friction X , which is the major contributor to the NHC strength, lags PDO+/IPO+ by 10–15 years and leads PDO–/IPO– by 10 years. This is consistent with the 10-yr AMO+ lead over PDO–/IPO– and 15-yr AMO+ lag over PDO+/IPO+ (d'Orgeville and Peltier 2007; see also Table S1). This suggests that the HC strengthens together with Walker circulation as the Pacific tropical zonal SST gradient weakens (PDO–, IPO–), consistent with (2) above, and also previous studies (e.g., Trenberth and Shea 1987).

Overall, we find that the coupled Atlantic–Pacific multidecadal variability (AMO, IPO, PDO) could be responsible for the recent Hadley cell strengthening and its variability (especially in the SH) through the mechanisms discussed above, although misrepresentation of the diabatic heating in reanalyses could contribute as well (section 4a; see also Chemke and Polvani 2019). This can be seen not only through the correlations (discussed above) but also through (multi)decadal variability in the time series (Fig. 8; see also Fig. S12). This reveals a weakening of the Hadley cell between 1950 and 1980 as well as after ~ 2002 (much like the AMO; see also Frajka-Williams et al. 2017) and strengthening between 1980 and 2002. This suggests that in the coming decades the Hadley cells might weaken further as AMO reaches its negative phase. It is, however, important to note that the reanalysis data have their limitations (as and therefore further studies with longer paleoclimate data records and long model runs are needed to solidify such conclusions).

5. Conclusions and outlook

The recent HC strengthening in most of the reanalyses is opposite to the well-accepted HC weakening as a response to the increasing atmospheric CO₂ concentration. Motivated by that, we have used a variety of methods (precipitation datasets, reanalyses, indices of interannual–multidecadal variability, the Kuo–Eliassen equation) in this study to assess whether the Hadley circulation strengthening in ERA5 is a possibly artificial trend (i.e., a result of latent heat biases) or a manifestation of the multidecadal variability.

The extended Kuo–Eliassen equation has been derived without quasigeostrophic assumptions, which is important for more accurate estimates of contributions to the atmospheric overturning circulation strengths. The equation has then been used for studying the relative contributions of different mechanisms to the HC trends and variability.

Our results indicate that historically diabatic processes have driven Hadley circulation variability (Fig. 2) and we expect that this relationship will continue to hold also in the future. We demonstrate that the strengthening of both HCs prior to 2000s and the NHC weakening and the SHC stagnation afterward are mostly due to the meridional gradient of diabatic heating Q_ϕ between the ascending and descending branches of the HC and that the diabatic heating is dominated by the latent heating component (Fig. 4), which is consistent with the findings of Chemke and Polvani (2019). Furthermore, we have verified that the meridional gradient of diabatic heating Q_ϕ and the mean meridional gradients of the zonal-mean precipitation P_ϕ (ERA5 and GPCP) between the ascending and the descending branches of the HC show compatible signs of the trend. They also exhibit a high correlation with the HC strength (Figs. 6 and 7). However, the ERA5 precipitation trend in the tropics overestimates the observed increasing trend in GPCP (1979–2018), but it is aligned with that in TRMM over the shorter period (1998–2018). Our results thus signify that the strengthening of both HCs in ERA5 is likely partly an artifact of misrepresentation of latent heating or any other systematic error, and partly a short-term snapshot of the multidecadal variability.

Recent studies have shown that moving into the future static stability will become the most important mechanism in driving the weakening of the northern Hadley cell strength (Chemke and Polvani 2020). However, no significant impact of static stability on the HC variability and trends has been found in our analysis of the historical reanalysis data.

While past studies have attributed the observed HC widening to long-term variability (PDO) (Vaugh et al. 2018; Allen and Kovilakam 2017; Grise et al. 2019), no study has yet attributed the changes in the HC strength to the Atlantic multidecadal oscillation (AMO), which describes the long-term variability of the SST distribution in the North Atlantic. We have found that the variability of the Hadley cell strength in ERA5 strongly matches the AMO index ($r = 0.77$ for NHC and 0.85 for SHC); that is, it is consistent with multidecadal variability of the coupled atmosphere–ocean system. For the

SHC, this is further confirmed by other long- to medium-range reanalyses (NOAA-20CR, ERA-20C, NCEP–NCAR), while the alignment of NHC and AMO is an isolated feature of the ERA5 reanalysis. However, we speculate that the SST-driven reanalyses (NOAA-20CR and ERA-20C) may struggle to adequately force the NHC, as there is a relatively smaller portion of ocean in the Northern Hemisphere than in the Southern Hemisphere.

Based on the results presented above, and the work of Li et al. (2016) and other studies, we propose a mechanism for the long-term Hadley cell variability. The mechanism is based on 1) the meridional gradients of SSTs that directly modulate meridional gradients in the tropical diabatic heating and precipitation (directly following from the Kuo–Eliassen budget) and 2) the zonal SST gradients that ultimately link the Pacific and Atlantic atmosphere–ocean circulations. The suggested mechanism for the HC strengthening (conversely for weakening) is as follows (Fig. 10):

- 1) During AMO+ there is a warming of the tropical Atlantic and milder warming (cooling) of the subtropical Atlantic. These SST anomalies change both zonal (interbasin) and meridional SST gradients.
- 2) The meridional SST gradients lead to stronger gradients in latent heat flux, diabatic (latent) heating, and precipitation. Tropical precipitation increases roughly exponentially with column atmospheric water vapor, which scales by the saturation specific humidity of the tropical ocean sea surface temperature (SST) (He et al. 2018; Good et al. 2020).
- 3) The gradient of latent (diabatic) heating directly impacts the Hadley cell in the Atlantic: the stronger the gradient of diabatic heating, the stronger the Hadley cell. This is the direct response.
- 4) Increased tropical SSTs in the Atlantic lead to stronger interbasin zonal SST gradients (Wang 2006), which enhance easterlies in the western Pacific and lead to enhanced latent heating over the Maritime Continent (Li et al. 2016, their Fig. 3a). This ultimately leads to basinwide enhanced easterlies (and trades) in the Pacific and through Bjerknes feedback to colder SST anomalies in the eastern Pacific, enhancing the Walker circulation (Li et al. 2016, their Fig. 3b), and strengthening the Hadley circulation. This is the remote response, which dominates the global HC (Fig. S13).

Note, however, that the utilized reanalysis data have some limitations. For example, they have often been deemed unsuitable for the estimation of long-term climate trends and low-frequency variability (D’Agostino and Lionello 2017), especially in the tropics (Žagar et al. 2020). However, the reanalyses are steadily improving, and in the most recent ERA5 (used here), the datasets that describe the observed low-frequency variability accurately were carefully included (Hersbach et al. 2020), thus allowing us to analyze its impact on the long-term HC variability.

For these reasons, further work is necessary to test the suggested mechanism (steps 1 to 4 enumerated above) in the

longer data record (e.g., paleoclimate data) and using climate models and to further elucidate the exact mechanisms responsible for the long-term Hadley cell variability. Other teleconnection patterns may also play an important role and should therefore be studied in more detail in the future. Our work also reaffirms that the meridional SST gradients are a major source of uncertainty in the future climate projections of the tropical circulation (Gastineau et al. 2009; Ma and Xie 2013; Davis and Birner 2017).

Further exploration of the AMO and the Hadley circulation cause-and-effect interplay should utilize modern reanalyses and climate models to separate the AMO impact on the Atlantic and Pacific Hadley cells, as well as the available decomposition tools (e.g., Žagar et al. 2015) to further validate the Gill-type response to AMO-related Atlantic heating (Li et al. 2016).

Acknowledgments. We thank the three anonymous reviewers for their helpful and constructive comments that helped improve the original manuscript considerably. We also thank Gregor Skok for helpful discussions. ŽŽ is funded by the Slovenian Research Agency project J1-9431. ŽŽ and MP are supported by ARRS Programme P1-0188. LB is supported by Trond Mohn Foundation (project BCPU, Grant BFS2018TMT01).

Data availability statement. GPCP precipitation data and climate indices are provided by the NOAA/OAR/ESRL PSL, Boulder, Colorado, USA, from their Web site at <https://psl.noaa.gov/>. The TMPA data were provided by the NASA/Goddard Space Flight Center's Mesoscale Atmospheric Processes Laboratory and PPS, which develop and compute the TMPA as a contribution to TRMM. The ERA-Interim, ERA-20C, and CERA-20C datasets are available from <http://www.ecmwf.int>. ERA5 data are available from the Copernicus Climate Data Store (CDS) at <https://cds.climate.copernicus.eu/>. The NOAA-20CR reanalysis dataset is available at https://psl.noaa.gov/data/20thC_Rean/. NCEP/NCAR reanalysis data are available from <https://psl.noaa.gov/data/gridded/data.ncep.reanalysis.html>. HadISST data are available from the Met Office Hadley Centre at <https://www.metoffice.gov.uk/hadobs/hadisst/data/download.html>. The code for Kuo-Eliassen decomposition is publicly available at <https://github.com/mpikovnik/Evaluating-contributions-to-global-Hadley-cell-using-Kuo-Eliassen-equation> and published in the Zenodo repository: <https://zenodo.org/record/6349274> Other scripts are available upon request.

APPENDIX A

Derivation of the Extended Kuo–Eliassen Equation

Our derivation of the extended Kuo–Eliassen equation initially follows that of Peixoto and Oort (Peixoto and Oort 1992). The basic equations governing the atmospheric flow are written in the spherical pressure coordinate system. Since the Hadley circulation is predominantly meridional and exhibits significant zonal symmetry, we can

write any quantity A as a sum of the zonally and temporally averaged part $[A]$ and the departure from this average A' , such that $A = [A] + A'$. The basic equations then read as follows:

- 1) the zonally averaged momentum equation:

$$\frac{\partial [u]}{\partial t} = -\frac{\partial([u][v]\cos^2\phi)}{R\cos^2\phi\partial\phi} - \frac{\partial([u'v']\cos^2\phi)}{R\cos^2\phi\partial\phi} - \frac{\partial([u][\omega])}{\partial p} - \frac{\partial([u'\omega'])}{\partial p} + f[v] + [F_\lambda], \quad (\text{A1})$$

- 2) the zonally averaged thermodynamic equation:

$$\frac{\partial [\theta]}{\partial t} = -\frac{\partial([v][\theta]\cos\phi)}{R\cos\phi\partial\phi} - \frac{\partial([v'\theta']\cos\phi)}{R\cos\phi\partial\phi} - \frac{\partial([\omega][\theta])}{\partial p} - \frac{\partial[\omega'\theta']}{\partial p} + \left(\frac{p_0}{p}\right)^{R_d/c_p} \frac{[Q]}{c_p}, \quad (\text{A2})$$

- 3) the zonally averaged mass continuity equation:

$$\frac{\partial([v]\cos\phi)}{R\cos\phi\partial\phi} + \frac{\partial[\omega]}{\partial p} = 0, \quad (\text{A3})$$

- 4) the thermal wind equation:

$$f \frac{\partial [u]}{\partial p} = \frac{1}{\rho[\theta]} \frac{\partial[\theta]}{R\partial\phi}. \quad (\text{A4})$$

Here, $R = 6371$ km is Earth's radius, $R_d = 287$ J kg⁻¹ K⁻¹ is the gas constant of dry air, $c_p = 1004$ J kg⁻¹ K⁻¹ is specific heat at constant pressure for dry air, and $p_0 = 1013.25$ hPa is mean-sea level pressure, while u denotes the zonal wind component v the meridional wind component, θ is potential temperature, and ω is pressure velocity (unit: Pa s⁻¹). In Eq. (A2), $[Q]/c_p = [J]$ is the heating rate (unit: K s⁻¹).

Within the traditional quasigeostrophic approximation (Rossby number $Ro \ll 1$), most terms involving ω are neglected in the above equation, yielding a much simpler set of equations. However in the tropics, ω terms are non-negligible, despite the Rossby number remaining low for planetary-scale circulation. Using the mass continuity Eq. (A3), we define a streamfunction ψ , such that the zonally averaged vector $[\mathbf{v}] = ([v], [\omega])$ is perpendicular to the streamfunction gradient ($[\mathbf{v}] \cdot \nabla\psi = 0$) everywhere on the pressure–latitude plane. This yields

$$[v] = \frac{g}{2\pi R \cos\phi} \frac{\partial\psi}{\partial p} \quad (\text{A5})$$

and

$$[\omega] = -\frac{g}{2\pi R \cos\phi} \frac{\partial\psi}{R\partial\phi}. \quad (\text{A6})$$

Next, we differentiate the thermal wind relationship (A4) over time (i.e., $\partial/\partial t$), change the order of partial derivatives, and finally plug in Eqs. (A1) and (A2) to obtain an extended Kuo–Eliassen equation:

$$\begin{aligned}
 & \underbrace{f^2 \frac{g}{2\pi R \cos \phi} \frac{\partial^2 \psi}{\partial p^2}}_{L_f} + \underbrace{\frac{g}{2\pi R} \frac{\partial}{R \partial \phi} \left(\frac{1}{R \cos \phi} \frac{\partial \psi}{\partial \phi} S^2 \right)}_{L_{S^2}} + \underbrace{\frac{g}{2\pi R} \frac{R_d}{p} \frac{\partial}{R \partial \phi} \left(\frac{\partial [T]}{R \cos \phi} \frac{\partial \psi}{\partial p} \right)}_{L_{T_\phi}} \\
 & + f \underbrace{\frac{g}{2\pi R \cos \phi} \left(\frac{\partial [u]}{\partial p} \frac{\partial^2 \psi}{R \partial \phi \partial p} + \frac{\partial^2 [u]}{\partial p^2} \frac{\partial \psi}{R \partial \phi} - \frac{\partial^2 ([u] \cos \phi)}{R \cos \phi} \frac{\partial \psi}{\partial p} - \frac{\partial ([u] \cos \phi)}{R \cos \phi} \frac{\partial^2 \psi}{\partial p^2} \right)}_{L_{u\psi}} \\
 & = \underbrace{\frac{R_d}{p} \frac{\partial [J]}{R \partial \phi}}_{D_{Q_\phi}} - \underbrace{\frac{R_d}{p} \frac{\partial}{R \partial \phi} \left(\frac{\partial ([v' T'] \cos \phi)}{R \cos \phi} \right)}_{D_{v'T'}} - \underbrace{f \frac{\partial [F_\lambda]}{\partial p}}_{D_X} + \underbrace{f \frac{\partial^2 ([u' v'] \cos^2 \phi)}{R \cos^2 \phi \partial p \partial \phi}}_{D_{u'v'}} \\
 & + f \underbrace{\frac{\partial^2 [u' \omega']}{\partial p^2}}_{D_{u'\omega'}} - \underbrace{\frac{R_d}{p} \left(\frac{p}{p_0} \right)^{R_d/c_p} \frac{\partial}{R \partial \phi} \frac{\partial [\omega' \theta']}{\partial p}}_{D_{\omega'\theta'}}, \tag{A7}
 \end{aligned}$$

where $f = 2\Omega \sin \phi$ is the Coriolis parameter, p_0 is mean-sea level pressure, R_d is specific gas constant for dry air, c_p is specific heat capacity, θ is potential temperature

$$S^2 = - \left\{ \frac{1}{[\rho][\theta]} \right\} \left(\frac{\partial [\theta]}{\partial p} \right) = - \left(\frac{R_d}{p} \right) \left(\frac{\partial [T]}{\partial p} \right) - \left(\frac{R_d}{c_p} \right) \left(\frac{[T]}{p} \right)$$

is static stability, square brackets denote zonal and seasonal (yearly) mean, and a prime denotes deviations therefrom.

Following Chemke and Polvani (2019), Eq. (A7) can be written in a simplified form as

$$L\psi = D_{Q_\phi} + D_{v'T'} + D_X + D_{u'v'} + D_{u'\omega'} + D_{\omega'\theta'}, \tag{A8}$$

where L is an elliptic second-order linear differential operator, and a function of stability, the Coriolis parameter, pressure–latitudinal distribution of zonal-mean zonal wind $[u]$, and zonal-mean (potential) temperature, that is,

$$L(t) = L_f + L_{S^2}(t) + L_{T_\phi}(t) + L_{u\psi}(t). \tag{A9}$$

Forcing terms are on the RHS: D_{Q_ϕ} is meridional gradient of diabatic heating (both condensational and radiative), D_X is friction, $D_{v'T'}$ meridional eddy heat fluxes, $D_{u'v'}$ meridional eddy momentum fluxes, and $D_{u'\omega'}$ and $D_{\omega'\theta'}$ vertical eddy heat and momentum fluxes. Primes denote deviations from monthly and zonal average, whereas square brackets denote annual zonal average (or seasonally, when we compute trends of seasonal-mean Hadley circulation);

- meridional and vertical heat and momentum fluxes ($[v' T']$, $[u' v']$, $[\omega' \theta']$, $[u' \omega']$) are computed from daily reanalysis data, where the primes denote deviation from moving monthly and zonal average, whereas square brackets denote annual zonal average (or seasonally, when we compute trends of seasonal-mean Hadley circulation);
- zonally averaged friction $[F_\lambda]$ is computed from zonally averaged momentum equation, Eq. (A1), with $\partial [u] / \partial t = 0$, which yields

$$\begin{aligned}
 [F_\lambda] &= \frac{\partial ([u][v] \cos^2 \phi)}{R \cos^2 \phi \partial \phi} + \frac{\partial ([u' v'] \cos^2 \phi)}{R \cos^2 \phi \partial \phi} \\
 &+ \frac{\partial ([u][\omega])}{\partial p} + \frac{\partial ([u' \omega'])}{\partial p} - f[v]; \tag{A10}
 \end{aligned}$$

- diabatic heating J is computed as a thermodynamic residual in the temperature conservation equation using daily data:

$$J = \frac{\partial T}{\partial t} + u \frac{\partial T}{R \cos \phi \partial \lambda} + v \frac{\partial T}{R \partial \phi} + \omega \frac{\partial T}{\partial p} - \frac{\omega T R_d}{p c_p}. \tag{A11}$$

Then J is zonally averaged over the year/season to obtain $[J]$.

The extended KE equation, Eq. (3), is solved numerically using a linear matrix system solver, which uses lower–upper (LU) decomposition.

APPENDIX B

Estimating the Contributions of Physical Processes to the Changes in the HC Strength

The contributions of different physical processes to the changes of HC strength are estimated based on Kim and Lee (2001) and Chemke and Polvani (2019). The linear operator is expanded as $L(t) = L_0 + \delta L(t)$, where L_0 denotes a reference operator (corresponding to year 1979) and $\delta L(t)$ deviation therefrom. Similarly, the forcing terms are decomposed as $D(t) = D_0 + \delta D(t)$ [where $D(t)$ is a sum of all forcing terms] and $\psi(t) = \psi_0 + \delta \psi(t)$. Accounting for $L_0 \psi_0 = D_0$, we then rewrite Eq. (3) as

$$\begin{aligned}
 L_0 \delta \psi &= \delta D - \delta L \psi_0 - \delta L \delta \psi \\
 &= \delta D_{Q_\phi} + \delta D_{v'T'} + \delta D_X + \delta D_{u'v'} \\
 &+ \delta D_{u'\omega'} + \delta D_{\omega'\theta'} - \delta L \psi_0 - \delta L \delta \psi. \tag{B1}
 \end{aligned}$$

Expressing $\delta\psi$ as a sum of different contributions

$$\delta\psi = \delta\psi_{Q_\phi} + \delta\psi_{v'T'} + \delta\psi_X + \delta\psi_{u'v'} + \delta\psi_{u'w'} + \delta\psi_{w'\theta'} + \delta\psi_{S^2, u_{p\phi}, T_\phi} + \delta\psi_{\text{res}}, \quad (\text{B2})$$

we obtain

$$\begin{aligned} L_0 \delta\psi_{Q_\phi} &= \delta D_{Q_\phi} \\ L_0 \delta\psi_{v'T'} &= \delta D_{v'T'} \\ L_0 \delta\psi_X &= \delta D_X \\ L_0 \delta\psi_{u'v'} &= \delta D_{u'v'} \\ L_0 \delta\psi_{u'w'} &= \delta D_{u'w'} \\ L_0 \delta\psi_{w'\theta'} &= \delta D_{w'\theta'} \\ L_0 \delta\psi_{S^2, u_{p\phi}, T_\phi} &= -\delta L \psi_0 \\ L_0 \delta\psi_{\text{res}} &= -\delta L \delta\psi. \end{aligned} \quad (\text{B3})$$

The residual term $\delta\psi_{\text{res}}$ is computed as

$$\underbrace{(L_0 + \delta L)}_L \delta\psi_{\text{res}} = -\delta L \left(\delta\psi_{Q_\phi} + \delta\psi_{v'T'} + \delta\psi_X + \delta\psi_{u'v'} + \delta\psi_{u'w'} + \delta\psi_{w'\theta'} + \delta\psi_{S^2, u_{p\phi}, T_\phi} \right). \quad (\text{B4})$$

Since L_f in Eq. (A9) is constant in time, $\delta L = \delta L_{S^2} + \delta L_{u_{p\phi}} + \delta L_{T_\phi}$ and $\delta\psi_{S^2, u_{p\phi}, T_\phi} = \delta\psi_{S^2} + \delta\psi_{u_{p\phi}} + \delta\psi_{T_\phi}$, it follows that

$$\begin{aligned} L_0 \delta\psi_{S^2} &= -\delta L_{S^2} \psi_0 \\ L_0 \delta\psi_{u_{p\phi}} &= -\delta L_{u_{p\phi}} \psi_0 \\ L_0 \delta\psi_{T_\phi} &= -\delta L_{T_\phi} \psi_0, \end{aligned} \quad (\text{B5})$$

where $\delta L_j(t) = L_j(t) - L_{j0}$ for $j = S^2, u_{p\phi}$, and T_ϕ .

Following Eqs. (B3) and (B5), we obtain streamfunction change $\delta\psi_j(t)$ from the reference field ψ_{j0} for each year/season $t \in [1979, 2018]$, and for each index $j = Q_\phi, S^2, u_{p\phi}, T_\phi, v'T', X, u'v', u'w', w'\theta'$, and the residual. The contribution of a certain physical process (e.g., diabatic heating Q_ϕ , static stability S^2 , ...) at time t , to the change of HC strength $\langle \delta\psi \rangle(t)$ is obtained using the same data-adaptive spatial averaging, $\langle \delta\psi_{Q_\phi} \rangle(t), \langle \delta\psi_{S^2} \rangle(t), \dots$, that is performed to average certain Hadley cells $\psi(t)$ [i.e., $\langle \delta\psi \rangle(t)$ following Eq. (2)]. The contributions $\langle \delta\psi_{Q_\phi} \rangle(t), \langle \delta\psi_{S^2} \rangle(t), \dots$ are then simply denoted as Q_ϕ, S^2, \dots hereafter.

For each time series $\langle \delta\psi_j \rangle(t)$ we compute its linear trend $\Delta \langle \delta\psi_j \rangle / \Delta t$, and then sum it up to obtain the total trend [following Eq. (B2)] as

$$\frac{\Delta \langle \delta\psi \rangle}{\Delta t} = \sum_j \frac{\Delta \langle \delta\psi_j \rangle}{\Delta t}. \quad (\text{B6})$$

REFERENCES

- Adler, R., and Coauthors, 2018: The Global Precipitation Climatology Project (GPCP) monthly analysis (new version 2.3) and a review of 2017 global precipitation. *Atmosphere*, **9**, 138, <https://doi.org/10.3390/atmos9040138>.
- Allen, R. J., and M. Kovilakam, 2017: The role of natural climate variability in recent tropical expansion. *J. Climate*, **30**, 6329–6350, <https://doi.org/10.1175/JCLI-D-16-0735.1>.
- Bony, S., G. Bellon, D. Klocke, S. Sherwood, S. Fermepin, and S. Denvil, 2013: Robust direct effect of carbon dioxide on tropical circulation and regional precipitation. *Nat. Geosci.*, **6**, 447–451, <https://doi.org/10.1038/ngeo1799>.
- Burls, N. J., and A. V. Fedorov, 2017: Wetter subtropics in a warmer world: Contrasting past and future hydrological cycles. *Proc. Natl. Acad. Sci. USA*, **114**, 12 888–12 893, <https://doi.org/10.1073/pnas.1703421114>.
- Chemke, R., 2021: Future changes in the Hadley circulation: The role of ocean heat transport. *Geophys. Res. Lett.*, **48**, e2020GL091372, <https://doi.org/10.1029/2020GL091372>.
- , and L. M. Polvani, 2019: Opposite tropical circulation trends in climate models and in reanalyses. *Nat. Geosci.*, **12**, 528–532, <https://doi.org/10.1038/s41561-019-0383-x>.
- , and —, 2020: Elucidating the mechanisms responsible for Hadley cell weakening under $4 \times \text{CO}_2$ forcing. *Geophys. Res. Lett.*, <https://doi.org/10.1029/2020GL090348>.
- Chou, C., T. C. Wu, and P. H. Tan, 2013: Changes in gross moist stability in the tropics under global warming. *Climate Dyn.*, **41**, 2481–2496, <https://doi.org/10.1007/s00382-013-1703-2>.
- Chung, E. S., A. Timmermann, B. J. Soden, K. J. Ha, L. Shi, and V. O. John, 2019: Reconciling opposing Walker circulation trends in observations and model projections. *Nat. Climate Change*, **9**, 405–412, <https://doi.org/10.1038/s41558-019-0446-4>.
- D'Agostino, R., and P. Lionello, 2017: Evidence of global warming impact on the evolution of the Hadley circulation in ECMWF centennial reanalyses. *Climate Dyn.*, **48**, 3047–3060, <https://doi.org/10.1007/s00382-016-3250-0>.
- Davis, N., and T. Birner, 2017: On the discrepancies in tropical belt expansion between reanalyses and climate models and among tropical belt width metrics. *J. Climate*, **30**, 1211–1231, <https://doi.org/10.1175/JCLI-D-16-0371.1>.
- Dee, D. P., and Coauthors, 2011: The ERA-Interim reanalysis: Configuration and performance of the data assimilation system. *Quart. J. Roy. Meteor. Soc.*, **137**, 553–597, <https://doi.org/10.1002/qj.828>.
- d'Orgeville, M., and W. R. Peltier, 2007: On the Pacific decadal oscillation and the Atlantic multidecadal oscillation: Might they be related? *Geophys. Res. Lett.*, **34**, L23705, <https://doi.org/10.1029/2007GL031584>.
- Enfield, D. B., A. M. Mestas-Nuñez, and P. J. Trimble, 2001: The Atlantic multidecadal oscillation and its relation to rainfall and river flows in the continental U.S. *Geophys. Res. Lett.*, **28**, 2077–2080, <https://doi.org/10.1029/2000GL012745>.
- England, M. H., and Coauthors, 2014: Recent intensification of wind-driven circulation in the Pacific and the ongoing warming hiatus. *Nat. Climate Change*, **4**, 222–227, <https://doi.org/10.1038/nclimate2106>.
- Frajka-Williams, E., C. Beaulieu, and A. Duchez, 2017: Emerging negative Atlantic multidecadal oscillation index in spite of warm subtropics. *Sci. Rep.*, **7**, 11224, <https://doi.org/10.1038/s41598-017-11046-x>.
- Gastineau, G., L. Li, and H. Le Treut, 2009: The Hadley and Walker circulation changes in global warming conditions described by idealized atmospheric simulations. *J. Climate*, **22**, 3993–4013, <https://doi.org/10.1175/2009JCLI2794.1>.
- Good, P., R. Chadwick, C. E. Holloway, J. Kennedy, J. A. Lowe, R. Roehrig, and S. S. Rushley, 2020: High sensitivity of tropical precipitation to local sea-surface temperature. *Nature*, **589**, 408–414, <https://doi.org/10.1038/s41586-020-2887-3>.

- Green, B., J. Marshall, and A. Donohoe, 2017: Twentieth century correlations between extratropical SST variability and ITCZ shifts. *Geophys. Res. Lett.*, **44**, 9039–9047, <https://doi.org/10.1002/2017GL075044>.
- Grise, K. M., and Coauthors, 2019: Recent tropical expansion: Natural variability or forced response? *J. Climate*, **32**, 1551–1571, <https://doi.org/10.1175/JCLI-D-18-0444.1>.
- Hausfather, Z., H. F. Drake, T. Abbott, and G. A. Schmidt, 2020: Evaluating the performance of past climate model projections. *Geophys. Res. Lett.*, **47**, e2019GL085378, <https://doi.org/10.1029/2019GL085378>.
- He, J., N. C. Johnson, G. A. Vecchi, B. Kirtman, A. T. Wittenberg, and S. Sturm, 2018: Precipitation sensitivity to local variations in tropical sea surface temperature. *J. Climate*, **31**, 9225–9238, <https://doi.org/10.1175/JCLI-D-18-0262.1>.
- Held, I. M., and B. J. Soden, 2006: Robust responses of the hydrological cycle to global warming. *J. Climate*, **19**, 5686–5699, <https://doi.org/10.1175/JCLI3990.1>.
- Henley, B. J., J. Gergis, D. J. Karoly, S. Power, J. Kennedy, and C. K. Folland, 2015: A tripole index for the interdecadal Pacific oscillation. *Climate Dyn.*, **45**, 3077–3090, <https://doi.org/10.1007/s00382-015-2525-1>.
- Hersbach, H., and Coauthors, 2020: The ERA5 global reanalysis. *Quart. J. Roy. Meteor. Soc.*, **146**, 1999–2049, <https://doi.org/10.1002/qj.3803>.
- Hoskins, B. J., and G.-Y. Yang, 2021: The detailed dynamics of the Hadley cell. Part II: December–February. *J. Climate*, **34**, 805–823, <https://doi.org/10.1175/JCLI-D-20-0504.1>.
- , —, and R. M. Fonseca, 2020: The detailed dynamics of the June–August Hadley cell. *Quart. J. Roy. Meteor. Soc.*, **146**, 557–575, <https://doi.org/10.1002/qj.3702>.
- Hu, S., and A. V. Fedorov, 2018: Cross-equatorial winds control El Niño diversity and change. *Nat. Climate Change*, **8**, 798–802, <https://doi.org/10.1038/s41558-018-0248-0>.
- Hu, Y., H. Huang, and C. Zhou, 2018: Widening and weakening of the Hadley circulation under global warming. *Sci. Bull.*, **63**, 640–644, <https://doi.org/10.1016/j.scib.2018.04.020>.
- Huffman, G. J., E. F. Stocker, D. T. Bolvin, E. Nelkin, and R. Adler, 2019: TRMM version 7 3B42 and 3B43 data sets. accessed 12 December 2019, <https://disc2.gesdisc.eosdis.nasa.gov>.
- Kalnay, E., and Coauthors, 1996: The NCEP/NCAR 40-Year Reanalysis Project. *Bull. Amer. Meteor. Soc.*, **77**, 437–472, [https://doi.org/10.1175/1520-0477\(1996\)077<0437:TNYRP>2.0.CO;2](https://doi.org/10.1175/1520-0477(1996)077<0437:TNYRP>2.0.CO;2).
- Kang, S. M., C. Deser, and L. M. Polvani, 2013: Uncertainty in climate change projections of the Hadley circulation: The role of internal variability. *J. Climate*, **26**, 7541–7554, <https://doi.org/10.1175/JCLI-D-12-00788.1>.
- Kerr, R. A., 2000: A North Atlantic climate pacemaker for the centuries. *Science*, **288**, 1984–1985, <https://doi.org/10.1126/science.288.5473.1984>.
- Kim, H., and S. Lee, 2001: Hadley cell dynamics in a primitive equation model. Part II: Nonaxisymmetric flow. *J. Atmos. Sci.*, **58**, 2859–2871, [https://doi.org/10.1175/1520-0469\(2001\)058<2859:HCDIAP>2.0.CO;2](https://doi.org/10.1175/1520-0469(2001)058<2859:HCDIAP>2.0.CO;2).
- Knutson, T. R., and S. Manabe, 1995: Time-mean response over the tropical Pacific to increased CO₂ in a coupled ocean–atmosphere model. *J. Climate*, **8**, 2181–2199, [https://doi.org/10.1175/1520-0442\(1995\)008<2181:TMROTT>2.0.CO;2](https://doi.org/10.1175/1520-0442(1995)008<2181:TMROTT>2.0.CO;2).
- Krishnamurthy, L., and V. Krishnamurthy, 2016: Teleconnections of Indian monsoon rainfall with AMO and Atlantic tripole. *Climate Dyn.*, **46**, 2269–2285, <https://doi.org/10.1007/s00382-015-2701-3>.
- Laloyaux, P., and Coauthors, 2018: CERA-20C: A coupled reanalysis of the twentieth century. *J. Adv. Model. Earth Syst.*, **10**, 1172–1195, <https://doi.org/10.1029/2018MS001273>.
- Levine, A. F., D. M. Frierson, and M. J. McPhaden, 2018: AMO forcing of multidecadal Pacific ITCZ variability. *J. Climate*, **31**, 5749–5764, <https://doi.org/10.1175/JCLI-D-17-0810.1>.
- Levine, X. J., and T. Schneider, 2011: Response of the Hadley circulation to climate change in an aquaplanet GCM coupled to a simple representation of ocean heat transport. *J. Atmos. Sci.*, **68**, 769–783, <https://doi.org/10.1175/2010JAS3553.1>.
- Li, X., S.-P. Xie, S. T. Gille, and C. Yoo, 2016: Atlantic-induced pan-tropical climate change over the past three decades. *Nat. Climate Change*, **6**, 275–279, <https://doi.org/10.1038/nclimate2840>.
- Lu, J., G. Chen, and D. M. Frierson, 2008: Response of the zonal mean atmospheric circulation to El Niño versus global warming. *J. Climate*, **21**, 5835–5851, <https://doi.org/10.1175/2008JCLI2200.1>.
- Luo, J. J., G. Wang, and D. Dommenget, 2018: May common model biases reduce CMIP5’s ability to simulate the recent Pacific La Niña-like cooling? *Climate Dyn.*, **50**, 1335–1351, <https://doi.org/10.1007/s00382-017-3688-8>.
- Ma, J., and S.-P. Xie, 2013: Regional patterns of sea surface temperature change: A source of uncertainty in future projections of precipitation and atmospheric circulation. *J. Climate*, **26**, 2482–2501, <https://doi.org/10.1175/JCLI-D-12-00283.1>.
- McGregor, S., A. Timmermann, M. F. Stuecker, M. H. England, M. Merrifield, F.-F. Jin, and Y. Chikamoto, 2014: Recent Walker circulation strengthening and Pacific cooling amplified by Atlantic warming. *Nat. Climate Change*, **4**, 888–892, <https://doi.org/10.1038/nclimate2330>.
- Merlis, T. M., 2015: Direct weakening of tropical circulations from masked CO₂ radiative forcing. *Proc. Natl. Acad. Sci. USA*, **112**, 13 167–13 171, <https://doi.org/10.1073/pnas>.
- Mitas, C. M., and A. Clement, 2005: Has the Hadley cell been strengthening in recent decades? *Geophys. Res. Lett.*, **32**, L03809, <https://doi.org/10.1029/2004GL021765>.
- , and —, 2006: Recent behavior of the Hadley cell and tropical thermodynamics in climate models and reanalyses. *Geophys. Res. Lett.*, **33**, L01810, <https://doi.org/10.1029/2005GL024406>.
- Newman, M., and Coauthors, 2016: The Pacific decadal oscillation, revisited. *J. Climate*, **29**, 4399–4427, <https://doi.org/10.1175/JCLI-D-15-0508.1>.
- Nguyen, H., A. Evans, C. Lucas, I. Smith, and B. Timbal, 2013: The Hadley circulation in reanalyses: Climatology, variability, and change. *J. Climate*, **26**, 3357–3376, <https://doi.org/10.1175/JCLI-D-12-00224.1>.
- Nogueira, M., 2020: Inter-comparison of ERA-5, ERA-Interim and GPCP rainfall over the last 40 years: Process-based analysis of systematic and random differences. *J. Hydrol.*, **583**, 124632, <https://doi.org/10.1016/j.jhydrol.2020.124632>.
- Peixoto, J. P., and A. H. Oort, 1992: *Physics of Climate*. American Institute of Physics, 507 pp.
- Pikovnik, M., Ž. Zaplotnik, L. Boljka, and N. Žagar, 2021: Indices of the Hadley circulation strength and associated circulation trends. *Wea. Climate Dyn. Discuss.*, 1–25, <https://doi.org/10.5194/wcd-2021-50>.
- Poli, P., and Coauthors, 2016: ERA-20C: An atmospheric reanalysis of the twentieth century. *J. Climate*, **29**, 4083–4097, <https://doi.org/10.1175/JCLI-D-15-0556.1>.

- Quan, X.-W., H. F. Diaz, and M. P. Hoerling, 2004: Change in the tropical Hadley cell since 1950. *The Hadley Circulation: Present, Past and Future*. Springer, 85–120, https://doi.org/10.1007/978-1-4020-2944-8_4.
- Rayner, N. A., D. E. Parker, E. B. Horton, C. K. Folland, L. V. Alexander, D. P. Rowell, E. C. Kent, and A. Kaplan, 2003: Global analyses of sea surface temperature, sea ice, and night marine air temperature since the late nineteenth century. *J. Geophys. Res.*, **108**, 4407, <https://doi.org/10.1029/2002JD002670>.
- Rivas, M. B., and A. Stoffelen, 2019: Characterizing ERA-Interim and ERA5 surface wind biases using ASCAT. *Ocean Sci.*, **15**, 831–852, <https://doi.org/10.5194/os-15-831-2019>.
- Schneider, U., P. Finger, A. Meyer-Christoffer, E. Rustemeier, M. Ziese, and A. Becker, 2017: Evaluating the hydrological cycle over land using the newly-corrected precipitation Climatology from the Global Precipitation Climatology Centre (GPCP). *Atmosphere*, **8**, 52, <https://doi.org/10.3390/atmos8030052>.
- Seager, R., M. Cane, N. Henderson, D. E. Lee, R. Abernathy, and H. Zhang, 2019: Strengthening tropical Pacific zonal sea surface temperature gradient consistent with rising greenhouse gases. *Nat. Climate Change*, **9**, 517–522, <https://doi.org/10.1038/s41558-019-0505-x>.
- Seo, K.-H., D. M. W. Frierson, and J.-H. Son, 2014: A mechanism for future changes in Hadley circulation strength in CMIP5 climate change simulations. *Geophys. Res. Lett.*, **41**, 5251–5258, <https://doi.org/10.1002/2014GL060868>.
- Shepherd, T. G., 2014: Atmospheric circulation as a source of uncertainty in climate change projections. *Nat. Geosci.*, **7**, 703–708, <https://doi.org/10.1038/ngeo2253>.
- Simmons, A. J., 2022: Trends in the tropospheric general circulation from 1979 to 2022. *Wea. Climate Dyn. Discuss.*, <https://doi.org/10.5194/wcd-2022-19>.
- Slivinski, L. C., and Coauthors, 2021: An evaluation of the performance of the Twentieth Century Reanalysis version 3. *J. Climate*, **34**, 1417–1438, <https://doi.org/10.1175/JCLI-D-20-0505.1>.
- Sohn, B. J., and S.-C. Park, 2010: Strengthened tropical circulations in past three decades inferred from water vapor transport. *J. Geophys. Res.*, **115**, D15112, <https://doi.org/10.1029/2009JD013713>.
- Stachnik, J. P., and C. Schumacher, 2011: A comparison of the Hadley circulation in modern reanalyses. *J. Geophys. Res.*, **116**, D22102, <https://doi.org/10.1029/2011JD016677>.
- Stuecker, M. F., and Coauthors, 2020: Strong remote control of future equatorial warming by off-equatorial forcing. *Nat. Climate Change*, **10**, 124–129, <https://doi.org/10.1038/s41558-019-0667-6>.
- Tanaka, H. L., N. Ishizaki, and A. Kitoh, 2004: Trend and interannual variability of Walker, monsoon and Hadley circulations defined by velocity potential in the upper troposphere. *Tellus*, **56A**, 250–269, <https://doi.org/10.3402/tellusa.v56i3.14410>.
- Trenberth, K. E., and D. J. Shea, 1987: On the evolution of the southern oscillation. *Mon. Wea. Rev.*, **115**, 3078–3096, [https://doi.org/10.1175/1520-0493\(1987\)115<3078:OTEOTS>2.0.CO;2](https://doi.org/10.1175/1520-0493(1987)115<3078:OTEOTS>2.0.CO;2).
- , and J. T. Fasullo, 2013: An apparent hiatus in global warming? *Earth's Future*, **1**, 19–32, <https://doi.org/10.1002/2013EF000165>.
- Vallis, G. K., 2006: *Atmospheric and Oceanic Fluid Dynamics: Fundamentals and Large-Scale Circulation*. Cambridge University Press, 773 pp.
- , P. Zurita-Gotor, C. Cairns, and J. Kidston, 2015: Response of the large-scale structure of the atmosphere to global warming. *Quart. J. Roy. Meteor. Soc.*, **141**, 1479–1501, <https://doi.org/10.1002/qj.2456>.
- Wang, C., 2006: An overlooked feature of tropical climate: Inter-Pacific–Atlantic variability. *Geophys. Res. Lett.*, **33**, L12702, <https://doi.org/10.1029/2006GL026324>.
- , C. Deser, J.-Y. Yu, P. DiNezio, and A. Clement, 2017: El Niño and Southern Oscillation (ENSO): A review. *Coral Reefs of the Eastern Tropical Pacific*, P. Glynn et al., Eds., Springer, 85–106, https://doi.org/10.1007/978-94-017-7499-4_4.
- Watanabe, M., J. L. Dufresne, Y. Kosaka, T. Mauritsen, and H. Tatebe, 2020: Enhanced warming constrained by past trends in equatorial Pacific sea surface temperature gradient. *Nat. Climate Change*, **11**, 33–37, <https://doi.org/10.1038/s41558-020-00933-3>.
- Waugh, D. W., and Coauthors, 2018: Revisiting the relationship among metrics of tropical expansion. *J. Climate*, **31**, 7565–7581, <https://doi.org/10.1175/JCLI-D-18-0108.1>.
- Xia, Y., and Y. Huang, 2017: Differential radiative heating drives tropical atmospheric circulation weakening. *Geophys. Res. Lett.*, **44**, 10 592–10 600, <https://doi.org/10.1002/2017GL075678>.
- , Y. Hu, and J. Liu, 2020: Comparison of trends in the Hadley circulation between CMIP6 and CMIP5. *Sci. Bull.*, **65**, 1667–1674, <https://doi.org/10.1016/j.scib.2020.06.011>.
- Yue, S., and C. Wang, 2002: Applicability of prewhitening to eliminate the influence of serial correlation on the Mann-Kendall test. *Water Resour. Res.*, **38**, 4–1, <https://doi.org/10.1029/2001WR000861>.
- Žagar, N., A. Kasahara, K. Terasaki, J. Tribbia, and H. Tanaka, 2015: Normal-mode function representation of global 3-D data sets: Open-access software for the atmospheric research community. *Geosci. Model Dev.*, **8**, 1169–1195, <https://doi.org/10.5194/gmd-8-1169-2015>.
- , Ž. Zaplotnik, and K. Karami, 2020: Atmospheric subseasonal variability and circulation regimes: Spectra, trends and uncertainties. *J. Climate*, **33**, 9375–9390, <https://doi.org/10.1175/JCLI-D-20-0225.1/4991565/jclid200225.pdf>.
- Zhang, R., and T. L. Delworth, 2007: Impact of the Atlantic multidecadal oscillation on North Pacific climate variability. *Geophys. Res. Lett.*, **34**, L23708, <https://doi.org/10.1029/2007GL031601>.
- Zhang, Y., J. M. Wallace, and D. S. Battisti, 1997: ENSO-like interdecadal variability: 1900–93. *J. Climate*, **10**, 1004–1020, [https://doi.org/10.1175/1520-0442\(1997\)010<1004:ELIV>2.0.CO;2](https://doi.org/10.1175/1520-0442(1997)010<1004:ELIV>2.0.CO;2).
- Zhou, C., J. Lu, Y. Hu, and M. D. Zelinka, 2020: Responses of the Hadley circulation to regional sea surface temperature changes. *J. Climate*, **33**, 429–441, <https://doi.org/10.1175/JCLI-D-19-0315.1>.
- Zurita-Gotor, P., 2019a: The role of the divergent circulation for large-scale eddy momentum transport in the tropics. Part I: Observations. *J. Atmos. Sci.*, **76**, 1125–1144, <https://doi.org/10.1175/JAS-D-18-0297.1>.
- , 2019b: The role of the divergent circulation for large-scale eddy momentum transport in the tropics. Part II: Dynamical determinants of the momentum flux. *J. Atmos. Sci.*, **76**, 1145–1161, <https://doi.org/10.1175/JAS-D-18-0304.1>.
- , and P. Álvarez-Zapatero, 2018: Coupled interannual variability of the Hadley and Ferrel cells. *J. Climate*, **31**, 4757–4773, <https://doi.org/10.1175/JCLI-D-17-0752.1>.